

Near-Infrared Absolute Photometric Imaging of the Uranian System

Kevin H. Baines
Jet Propulsion Laboratory
California Institute of Technology
M/S 183-601
4800 Oak Grove Drive
Pasadena, California 91109
(818) 354-0481
FAX: (818) 393-4605
E-mail: kbaines@aloha.jpl.nasa.gov

Padmavati A. Yanamandra-Fisher
Jet Propulsion Laboratory
M/S 169-237
4800 Oak Grove Drive
Pasadena, California 91109

Larry A. Lebofsky
Lunar and Planetary Laboratory
University of Arizona
Tucson, Arizona 85721

Thomas W. Momary
Dept. of Earth and Space Sciences
University of California, Los Angeles
595 Circle Drive East
Los Angeles, California 90095-1562

William Golisch, Charles Kaminski,
NASA Infrared Telescope Facility,
2680 Woodlawn Drive
Honolulu, Hawaii 96822

and

Walter J. Wild
Dept of Astronomy & Astrophys.
University of Chicago
5640 S. Ellis Ave
Chicago, Illinois 60637

Submitted to *Icarus*, April 14, 1997

Revised December 19, 1997

Key Words: Uranus
Planetary Rings, Uranus
Satellites of Uranus
Spectrophotometry
Surfaces, Satellite

Manuscript Pages: 56
Number of Figures: 15
Number of Tables: 7

Proposed Running Head:

Near-Infrared Imagery of the Uranian System

Send Editorial Correspondence and Proofs to:

Dr. Kevin H. Baines

M/S 183-601

Jet Propulsion Laboratory

4800 Oak Grove Drive

Pasadena, Ca 91109

818-354-0481

E-mail: kbaines@aloha.jpl.nasa.gov

FAX: 818-393-4605

ABSTRACT

We report the first multi-filter set of absolutely-calibrated near-infrared images of Uranus, its rings, and three major satellites - Titania, Ariel, and Miranda. Along with imagery utilizing the canonical K filter bandpass (effective wavelength $2.20\ \mu\text{m}$), absolutely calibrated images of the uranian system are presented for the first time for three additional filter bandpasses: J ($1.27\ \mu\text{m}$), H ($1.62\ \mu\text{m}$) and in a narrow bandpass ($0.1\ \mu\text{m}$ full-width-at-half-maximum) centered at $1.73\ \mu\text{m}$ (hereafter designated H') particularly diagnostic of C-H stretch vibrational absorptions common in hydrocarbons. Multi-filter-derived spectra of the southern ring ansa including the bright apoapse of the dominant ϵ ring show no absorptions due to condensable volatiles, including water, ammonia, and light (high H:C) hydrocarbons. Plausible near-infrared spherical geometric and single-scattering particle albedos consistent with Voyager-derived phase functions range from 0.069 to 0.102 and 0.030 to 0.037, respectively. These are approximately 50% greater than visible values, consistent with the optical properties of charcoal, carbonaceous chondrite material, and the darkside of Iapetus, and consistent with the hypothesis that a primary component of the ring particles is high stoichiometric ratio C:H organics produced by charged-particle and/or photochemical weathering of methane clathrate and/or hydrocarbon ice material originating from nearby moonlets. Additional components consistent with the ring spectrum include silicates such as pyroxene, but not olivine. Analytical modelling of the ring structure indicates ϵ -ring near-infrared opacities of 0.37 ± 0.05 and 1.8 ± 0.3 at apoapsis and periapsis, respectively. Ariel is more than 25% brighter than Miranda and 15%

brighter than Titania at all near-infrared wavelengths. Comparisons with UV-visible spectra by Karkoschka (1997, *Icarus* 125, 348-363) show consistency with the hypothesis that the water-ice surfaces of Titania and Ariel are contaminated with low-reflectance, near-ir-reddened substances similar to the weathered high C:H material postulated for the uranian ring system. The relatively blue, near-infrared dark surface of Miranda (full-disk near-infrared albedo of ~ 0.22 at 2.4° phase angle) exhibits the greatest water ice absorption band-depth and the largest H- and K-filter brightness surge measured among the uranian satellites, consistent with (1) a markedly heterogeneous surface punctuated with localized outcroppings of relatively pure water ice and (2), as with Titania and Ariel, a surface composition dominated in the near-infrared by weathered high C:H material. The uranian disk shows marked latitudinal variability in tropospheric cloud structure, with a "polar cap" of aerosols lying within the planet's southern polar region. This is in sharp contrast with the stratospheric haze structure, which is nearly globally uniform.

1. INTRODUCTION

The uranian system is the nearest planetary system to the Sun exhibiting a significant abundance of hydrocarbons within the governing planet. Specifically, within the extensive tropospheres of both Uranus and Neptune, methane accounts for over 1.5% by volume and over 11% by mass of the gas content (Baines *et al.* 1995). The presence of substantial amounts of hydrocarbons in these planets indicates that carbon-containing planetesimals were a major planetary formation component for the outermost gas giants (Bodenheimer and Pollack 1986; Pollack *et al.* 1986; Baines *et al.* 1995). Yet, carbon-containing materials have not been specifically identified in the spectra of either the associated satellites or ring systems surrounding these major bodies, indicating that post-accretion processing - in particular, sublimation of low C:H material - probably has occurred.

The rings have thus far been spectro-photometrically observed only in the visible and in one near-infrared band. Both Voyager (*e.g.*, Smith *et al.* 1986; Ockert *et al.* 1987) and, more recently, the Hubble Space Telescope (Karkoschka 1997), have obtained visible images of the ring system in several colors. In addition, several studies of the rings have been made in the methane-sensitive near-infrared K-band (*e.g.*, Nicholson and Jones 1980; Matthews *et al.* 1982; Nicholson *et al.* 1983; Nicholson 1984). Yet, since observations have never been acquired simultaneously over both absorption-sensitive and nearby continuum wavelengths, no

information on the presence or abundances of pure hydrocarbon or water condensates can be inferred from these previous observations.

The identification of pure hydrocarbons within the rings or on satellite surfaces would place tight constraints on the ages of surface materials. Weathering by solar ultraviolet light, the solar wind, and magnetospheric ions changes both the composition and the spectrum of hydrocarbon ices in astronomically/geologically-short time scales (under 10 millennia; *e.g.*, Lanzerotti and Johnson 1987; Khare *et al.* 1993), quickly destroying tell-tale absorption features as the hydrocarbons blacken into a featureless spectrum of high stoichiometric ratio C:H materials. Hence, the identification of C-H absorptions within the rings would indicate the presence of exceedingly young, low C:H material, thus placing a significant constraint on the rate of ring replenishment from nearby moonlets (*e.g.*, Esposito and Colwell 1989) and indicating an active, evolving uranian ring and inner satellite system today.

Water ice is a major constituent of satellite surfaces, as spectrally identified in the near infrared by, for example, Cruikshank and Brown 1981, Brown and Cruikshank 1983, and Brown and Clark 1984. The identification of this constituent within the ring system would indicate a common formation/evolution scenario, at least for the relatively old parent moonlets supplying material to the relatively young ring system.

In this paper, we present for the first time absolutely-calibrated, high-spatial-resolution, multi-color near-infrared imagery of the uranian system, including the planet, the ring system, and three satellites - Ariel,

Miranda, and Titania. We also interpret these observations, specifically as they pertain to the distribution of hydrocarbon and water condensates within the uranian ring system. Section 2 presents the observations and data reduction procedures, particularly for retrieving the relatively faint ring system signal observed in Uranus-bright continuum J and H bands. Section 3 presents the observational results, describing the observed absolutely-calibrated I/F and full-disk spectra for the various bodies observed in the uranian system. Section 4 discusses the implication of these spectra for scenarios of satellite and ring system composition, formation, and evolution.

2. OBSERVATIONS AND DATA REDUCTION

2.1 Observations

Table I

Near-infrared images of Uranus were acquired at the NASA/Infrared Telescope Facility, Mauna Kea, Hawaii on July 10, August 10, and September 16, 1995. The observational instrumentation and settings were identical on all three dates. The 256*256 array near-infrared IRTF imager, NSFCAM, was used at its 0.15 arc-sec per pixel plate scale setting. Standard broadband J, H, K filters were employed (*c.f.* Table I) as well as a relatively narrow H' filter characterized by an effective wavelength of 1.73 μm and a full-width-at-half-maximum (FWHM) of 0.1 μm . These filters covered a number of strong spectral features of plausible condensables and gases in the uranian system. Among these filters, water ice preferentially absorbs within the H-filter centered at 1.62 μm , while

hydrocarbon ice and gas absorptions dominate at K - centered at $2.2\ \mu\text{m}$ - and at H'.

Table I summarizes the observations. On each night, the uranian system - consisting of the planet, its ring system, and several satellites - was observed at relatively low airmass. Each observation consisted of repeated sub-observations alternating between the target and the sky, the latter offset by one minute of arc to the north of the target.

For the August and September measurements, the nearby absolutely calibrated star EG141, also known as UKIRT Faint Star #34, was used to determine the absolute calibration of each image. Located just eleven degrees in Right Ascension and one degree in Declination from Uranus, repeated observations of this star also characterized the local sky transparency. At least one observation for each filter was obtained at an airmass close (typically <0.1 airmass) to that of the Uranus image, in order to minimize the flux error due to uncertainty in the derived extinction coefficient.

Out-of-focus flat-field images of the IRTF flat-field calibration target located on the IRTF dome were obtained for each wavelength on each night, both with the dome lights on and with the dome lights off, the latter to assess instrument-only dark current effects. To minimize non-linearities in images of the uranian system, integration times were limited to preserve a maximum electron count of less than 1500, *i.e.*, about 20% of the well depth and a value known to preserve linearity to within 5%. Nevertheless, array linearity was characterized for each night through

thermal imagery of an out-of-focus target located within the instrument optics. Observations were acquired over forty different integration times to characterize the response of the array to variations in the known number of thermal photons striking it.

2.2 Reduction Procedures

Standard data reduction procedures were used (*e.g.*, Bergstralh *et al.* 1981; Hammel *et al.* 1989). Each image was first linearized, utilizing the linearity coefficients derived from the linearity images. Sky observations were subtracted from each target observation, and then divided by the net flat-field image for the appropriate wavelength derived from differencing the lights-on and lights-off dome target images. For each pixel of uranian system imagery obtained in the August and September runs, the flux relative to the calibration star was determined, appropriately correcting for the variation in star/target atmospheric extinction via the extinction coefficients derived from the pair of star observations obtained for each filter. For the July images, used only to determine the near-infrared opposition brightness surge of Miranda, the images were scaled to the full-disk albedo of Uranus and its rings, which was observed to be nearly constant (to within 1%) between the August and September runs.

For the August and September observations, the absolute flux for each pixel of the uranian system was then determined utilizing the known EG141 flux (*c.f.* Guarnieri *et al.* 1991 and UKIRT faint star listing). In particular, a K magnitude of 12.989 ± 0.011 and J-K and H-K relative magnitudes of -0.170 ± 0.008 , and -0.070 ± 0.009 , respectively, were

adopted. Each pixel's flux was then scaled to the solar flux at Uranus via the measured solar flux of Arvesen *et al.* 1969. In these calculations, a measured plate scale of 0.1478 arc-secs per pixel was utilized, as determined by the observed relative pixel coordinates of several satellites and the center-of-disk of Uranus compared to their known relative positions as specified by the Nautical Almanac 1995.

The azimuthal ring brightness structure and the integrated full-disk ring system albedo could be readily determined for the K filter images. At 2.2- μm , scattered light from Uranus is dramatically reduced due to strong atmospheric methane absorption (*c.f.* Baines *et al.* 1993) which reduces the planet's brightness by a factor of 200 compared to J and H wavelengths. Indeed, in K, the median ring pixel brightness at almost all azimuths outshines the brightest pixel on the planet.

At other wavelengths, determination of ring brightness was hampered significantly by the scattered light from Uranus. Only the relatively sharp September images (point-spread-function FWHM < 0.6 arc-sec) were used to determine ring brightness for J, H, and H'. In these images, the bright ϵ -ring apoapsis was particularly well-placed near the elongated southern ansa (*c.f.* Figure 1), nearly 0.8 arc seconds further from the planet than in the east or west, further reducing contamination from scattered light. Nevertheless, corrections were required for scattered light from the disk of the planet and the telescope secondary mirror support structure ("spider"). This was accomplished utilizing the western (on the sky) profile for each band, which is clear of ring light at radial positions beyond 3.5 arc-secs corresponding to the maximum ring brightness within

FIGURE 1

the northern/southern ansae profiles (*c.f.*, Figures 2 and 3). From 3.5-4.7 arc-sec, the western profile was first subtracted directly from the ansae profiles. The profiles were compared at larger radial positions out to 6.6 arc seconds, and it was found that, for all filters, the southern spider profiles were uniformly greater than the western profiles. The southern ansae profiles were corrected by this offset, to obtain > 3.5 -arc-sec scattered-light-corrected profiles.

In the 2.5-3.5 arc-sec range encompassing the western ring, the ring brightness profiles for all filters were nearly identical. This enabled the near-Uranus portions of the northern and southern ansae J, H, and H' profiles also to be corrected for scattered light via western profile subtraction. The over-correction due to subtraction of the western ring flux itself from the southern/northern profiles was corrected by adding back western ring light observed in the uncontaminated K filter image. Finally, the southern spider offset noted above was included.

For J, H, and H' filters, the radially-integrated ring system brightness used to determine ring I/F was evaluated for the southern and northern ansae by integrating scattered-light-corrected north/south column profiles through the 10 rows of pixels which radially span the outer half of the ring system profile from 3.5-4.7 arc-secs. The integrated brightnesses were ratioed to that found for the 3.5-4.7 arc-sec profile of the K filter, and then multiplied by the radially-integrated K profile brightness evaluated over the entire ring profile from 2.5-4.7 arc-secs. For each ansa, the integrated profiles of five neighboring column profiles were averaged together for

improved signal/noise and to evaluate the photon statistical uncertainty of the measured ring brightness.

FIGURE 4

To transform the observed ring brightnesses to intrinsic I/F units, we adopted a southern ansa ϵ ring true anomaly of 208 degrees for our September 16, 1995 data, as ascertained from known ring ephemeris and confirmed by the position and movement of the observed K-filter peak ring brightness measured in the July, August, and September images (*c.f.*, Figure 4). In this analysis, we used the known ring precession rate (1.36325 degrees per day; French *et al.* 1991) and ϵ ring shape (*ibid*, Figure 25). Specifically, we adopted ϵ ring widths of 91.3 and 24.2 km for the southern and northern ansae, respectively. Similarly, the α and β ring widths were calculated utilizing their southern ansae true anomalies of 287 degrees and 3 degrees, respectively, yielding southern ansae widths of 6.6 km and 5.5 km, and northern ansae widths of 8.4 and 12.0 km for the α and β rings, respectively. For the remainder of the ring system, an azimuthally-constant 20.3-km composite width was adopted. This approach yields uranian ring system widths of 64.9 and 123.7 km on September 16, 1995 for the northern and southern ansae, respectively, and minimum and maximum widths of 58.6 and 130.0 km.

Observed brightnesses for each pixel were converted to intrinsic I/F values for the unresolved rings and satellites by accounting for the projected pixel size, in km units, at the distance of Uranus and the known size of the targets. For the ring ansae, ring I/F values were calculated from:

$$I/F = W_p \Sigma I/F' / W_a, \quad (1)$$

where W_p , the pixel width at Uranus for a 0.1478 arcs-sec per pixel plate scale, is 2053 km, W_a is the width of the ring ansa, and $\Sigma I/F'$ is the radially-integrated brightness along the observed ansa profile, as discussed above. For the satellites and Uranus, the full-disk albedos, p , utilized

$$p = W_p^2 \Sigma I/F' / (\pi r_s^2), \quad (2)$$

where r_s is the satellite/planet radius and $\Sigma I/F'$ is the integrated brightness over all pixels associated with the satellite/planet (typically, satellite fluxes were integrated out to a 1.4 arc-sec radius from the satellite center, encompassing approximately 300 pixels). Full-disk ring system evaluations used essentially the same equation, except that the satellite area term in the denominator was replaced with the explicit projected ring system area (accounting for the 38.1-degree tilt of the ring plane to the Earth-Uranus position vector) of $2.376 \times 10^7 \text{ km}^2$. Satellite albedo calculations assumed radii of 235.8, 578.9, and 788.9 km for Miranda, Ariel, and Titania, respectively (Brown *et al.* 1991; Table I). For Uranus, a radius of 25360 km was used.

Each image was geometrically registered utilizing the disk of Uranus for J and H filter images and the ring shape and extent for H' and K images. For the J and H filter observations, the images were photometrically stretched to saturate at 3% of the peak I/F. This corrected for the asymmetrical appearance of Uranus caused by the bright southern polar region offset to the east (on the sky) of the disk center.

2.3 Error Analysis

As discussed by Bergstralh *et al.* 1981, uncertainties can be deemed "fixed error" or "variable error" according to wavelength dependence. Fixed errors are those that do not depend on wavelength, and therefore do not affect the spectral character (*e.g.*, band depth, spectral slope) derived from a set of images. For our observations, the predominant sources of fixed error are pixel area, target dimension, and K-filter calibration of EG141 and, for the rings, of the ansae profiles upon which the other wavelength calibrations and profiles depend. Measurements of the plate scale conducted on several images over the three observing runs determined a pixel scale of 0.1478 ± 0.0010 arc-seconds per pixel, corresponding to a linear dimension fractional uncertainty of 0.0068 and pixel area fractional uncertainty of 0.0136. Ring width uncertainty is 1 km, based on the uncertainty of ignoring the potentially azimuthally-varying widths of the non- α, β, ϵ rings. This yields fractional uncertainties of 0.008 and 0.016 at the southern and northern ansae, respectively. Satellite radius fractional uncertainties are 0.005, 0.002, and 0.0035 for Miranda, Ariel, and Titania, respectively (Brown *et al.* 1991), doubling to 0.010, 0.004, and 0.007 areal uncertainties for satellite albedo calculations. K-filter EG141 uncertainty is 0.011 (Guarnieri *et al.* 1991). The K-profile uncertainty for the southern and northern ansae are 0.018 and 0.028, respectively, the standard deviation of five adjacent column profiles discussed above. The net fixed error, σ_{FE} , expressed in fractional units, is 0.026 and 0.037 for the derived southern and northern ring ansa I/F's, respectively, and 0.020, 0.018, and 0.019 for full-disk albedo estimates of Miranda, Ariel, and Titania. The full-disk albedo fixed-error for Uranus is 0.018.

The wavelength-dependent variable fractional error, $\sigma_{VE}(\lambda)$, can be expressed as

$$\sigma_{VE}^2(\lambda) = \sigma_{sol}^2(\lambda) + \sigma_{EG141}^2(\lambda) + \sigma_{flx}^2(\lambda) + \sigma_{ext}^2(\lambda) \quad (2),$$

where $\sigma_{sol}(\lambda)$ is the solar flux uncertainty, σ_{EG141} is the absolute flux uncertainty of the calibration star, σ_{flx} is the photon noise uncertainty of our measurements, including both the calibration star and the target, and σ_{ext} is the atmospheric extinction uncertainty. Generally, if the variation in sky transparency is large during the observations, then σ_{flx} may be replaced by the standard deviation of the measured sky variability (Bergstralh *et al.* 1981). Here, the sky transparency was quite steady during the five minute observation period, as evidenced by the invariance of the sky throughout each of the observing nights (Observations of Jupiter, Saturn, Neptune and their calibrators occurred for over three hours before and after the Uranus observations; all observations showed a steady sky). The photon noise thus predominates. For the ring observations, σ_{flx} also includes the uncertainty in scattered light reduction, due to both Uranus and the telescope spider.

σ_{ext} is defined as

$$\sigma_{ext}(\lambda) = \sigma_e(\lambda) \delta_a(\lambda) \ln(10)/2.5 \quad (3)$$

where $\delta_a(\lambda)$ is the airmass difference between Uranus and the nearest EG141 observation. Here $\sigma_e(\lambda)$ is calculated as the standard deviation of

the slope of the line which best fits the observed calibration star magnitude vs airmass.

$\sigma_{\text{sol}}(\lambda) < 0.012$ and $\sigma_{\text{EG141}}(\lambda) < 0.008$ for all filters. σ_{ext} is small (< 0.008) as well except for the J filter observations of September 16, where $\sigma_{\text{ext}}(\lambda) = 0.033$. For all filters except K, the dominant error source for the southern ring ansa is σ_{flx} , the ring photon noise/scattered light uncertainty. The photon noise component is determined from the standard deviation observed among five neighboring column traverses through the ansa. The scattered light component is similarly determined from five neighboring western row traverses spanning the radial range of the ansa. For the southern ansa, σ_{flx} ranges from 0.036 for the H' filter to 0.098 for J. Photon noise is significantly less (*i.e.*, 0.009) for the K filter, which is not affected by scattered light from Uranus. For the northern ansa, photon noise ranges from 0.028 for K to 0.243 for J.

Satellite photon noise is estimated as the southern ring ansa photon noise multiplied by the square-root of the ratio of satellite signal to southern ansa signal. The photon noise ranges from 0.008 to 0.045, 0.002 to 0.124, and 0.003 to 0.014 for Miranda, Titania, and Ariel, respectively, with the largest uncertainty pertaining to J, the smallest for K.

The net variable fractional errors for the southern and northern ring ansae range 0.016 to 0.108 and 0.031 to 0.247, respectively, with the smallest and largest values again pertaining to K and J. The satellite σ_{VE} range from 0.017 to 0.067 for Miranda and from 0.015 to 0.048 for Titania and Ariel. The composite error, encompassing both the variable and fixed

errors, range from 0.029 to 0.110 for the southern ansa and 0.046 to 0.249 for the northern ansa. Composite errors for Miranda, Titania, and Ariel range 0.025 - 0.068, 0.023 - 0.051, and 0.023 - 0.100, respectively. Except where noted, all error bars shown in the accompanying tables and figures include these composite errors, appropriately converted to I/F or full-disk albedo units.

3. RESULTS

3.1 *Uranus*

FIGURE 5

Meridional profiles (Figure 5) confirm the dichotomy readily observed in the images of Uranus (Figure 1): low flux level methane absorption band H' and K profiles are symmetric, while relatively bright profiles obtained in pseudo-continuum J and H bands are distinctly asymmetric. The absorption-band profiles primarily detect light reflected from stratospheric aerosols above the ~50 mbar level, and these images thus reveal that these high-altitude aerosols are distributed uniformly across the disk. The pseudo-continuum images detect additional aerosols residing throughout the lower stratosphere and troposphere down to approximately the 3-bar level (Baines *et al.* 1995). The asymmetry observed in these images thus reveals distinctive variability in the latitudinal distribution of tropospheric aerosols, with significantly enhanced cloud opacities at polar latitudes south of ~60 S. Details on cloud vertical profiles over the south pole, mid southern latitudes, and the equator, as revealed by these images are the subject of a subsequent paper.

3.2 Ring Spectra

FIGURE 6

Figure 6 shows the southern and northern ansae profiles for each of the filters. Integrating over these profiles and scaling as discussed in Section 2.2 results in the I/F spectra displayed in Table II. Within the uncertainty limits, both spectra are flat, showing no features indicative of pure water ice or low C:H hydrocarbon condensates. In particular, no increase in absorption is seen in the H' 1.73- μ m filter, which would be indicative of saturated alkanes and other high H:C hydrocarbons (*c.f.* Cloutis 1989; Schmitt *et al.* 1993).

The absence of 1.62- μ m absorption precludes pure (~99%) water frost as the only constituent of ring particle surfaces. This is consistent as well with the dark albedo of the ring particles. However, the absorption data alone does not preclude water ice as the predominant surface constituent. As demonstrated by Clark and Lucey 1984, a small admixture of dark material - consistent with the overall low ring albedo - readily masks water ice absorption features. Our spectrum, including error bars (*c.f.* Figure 7), admits a possible 20% band depth, although the nominal albedo values allow for just a 5% absorption. For our dark ring albedo, such absorptions are consistent with a wide range of admixtures of charcoal-like substances - from 0.1 to 99% by weight (*c.f.* Figure 3 of Clark and Lucey 1984) - although our nominal spectrum admits only admixtures greater than 50%.

FIGURE 7

A stronger case against water ice as the predominant ring constituent comes from the reddened color of the ring albedo which is qualitatively consistent with the 70% by weight charcoal admixture spectrum of Clark and Lucey 1984 (*c.f.* their Figure 2c). However, the spectral shape of the ring albedo is not consistent with spectra produced with smaller admixtures of charcoal (*e.g.*, 50% by weight). These spectra are all bluer, showing nearly steady decreases in reflectivity between 0.5 and 2.5 μm rather than the increase seen in the rings, as we now discuss.

Table III

Although quite dark in the near-infrared, the ring system is nevertheless ~50% brighter than at visible wavelengths measured by Voyager and the Hubble Space Telescope (*c.f.* Porco *et al.* 1987; Esposito *et al.* 1991; Karkoschka 1997). As shown in Table III and in the bottom spectrum of Figure 7, the full-disk albedo, $p(1^\circ)$, measured at a phase angle of 1.0° by both HST in July 1995 (Karkoschka 1997) and by us one month later, is less than 0.035 throughout the measured 0.36 - 2.2 μm spectral range, but rises more than 50% from 0.55 μm to 1.27 μm . This visible/near-ir dichotomy is consistent with laboratory measurements of charcoal (Brown 1983) and weathered, carbon-rich organic residue produced from high energy ion bombardment of frozen methane (Calcagno *et al.* 1985).

The visible-near-infrared spectral curve is similar to that of several other classes of dark objects scattered throughout the Solar System, including carbonaceous residue derived from the Murchison C2 chondritic meteorite and the dark hemisphere of Iapetus (*e.g.*, Cruikshank *et al.* 1983), as well as the asteroid Ida (Helfenstein *et al.* 1996). As shown in

FIGURE 8

Figure 8, all of these objects exhibit near-infrared brightnesses about 50% greater than observed in the visible. As illustrated in panel (a) of Figure 8, the ring spectral curve agrees particularly well with the Iapetus full-disk darkside spectral curve throughout the 0.34 - 2.2 μm spectral range, except at 0.91 μm . As shown in Ida's spectrum (panel c), this wavelength is particularly diagnostic of the common asteroidal refractories, olivine and pyroxene. The lack of a clear 1.73- μm absorption in the ring spectrum argues somewhat against pyroxene, as observed near 1.85 μm in Ida, although, due to the measurement uncertainty, it can not be ruled out. A greater inconsistency is the flatness of the ring spectrum from J to H, which eliminates olivine. The spectral curve of the ring is inconsistent as well with pure Iapetus darkside material uncontaminated by polar ice reflectance, as derived by Bell *et al.* (1985; *e.g.*, their Figure 9). This pure darkside component is characterized by a factor-of-three rise in spectral reflectance between 0.5 and 2.2 μm , as opposed to the 50% rise reported here. Thus the gross spectral character of the material observed on the surfaces of uranian ring particles is consistent with the average carbon-rich material/ice mixture found on the dark hemisphere of Iapetus (*c.f.* Wilson and Sagan 1995; Wilson and Sagan 1996), mixed with pyroxene. As noted below (Section 4.1), similarities in optical properties between the rings and Iapetus' dark side extends to the spherical geometric particle.

3.3 Ring Models

In order to constrain the near-infrared single-scattering albedo, ω_ϵ , and periapsis opacity, $\tau_{\epsilon,p}$, of the ϵ ring particles, the northern and southern ansae K-filter I/F's were fit to an isotropically-scattering

multiple-scattering model, utilizing our doubling-adding code previously used to analyze the vertical structure of Uranus and Neptune (*e.g.*, Baines and Bergstralh 1986; Baines and Hammel 1994). In this analysis, the azimuthally-varying opacities of the α , B, and ϵ rings, measured normal to the ring plane, were assumed to vary inversely with the individual ring widths, as necessary to conserve the cross-sectional integrated ring particle mass required for nearly-circular ring orbits. For the ϵ ring, ϖ_ϵ and $\tau_{\epsilon,p}$ were derived for various values of K, the ratio of non- ϵ -ring to ϵ -ring brightness at the northern ansa. Table IV and Figures 9-11 show these results.

FIGURE 9

Voyager visible imaging of the ring system (*e.g.*, French *et al.* 1991; Esposito *et al.* 1991) indicates that the non- ϵ ring component contributes about 30% of the brightness of the total ring system in the visible, corresponding to $K \sim 0.8 - 1.2$. Over this range, our derived near-infrared perihelion opacity, τ_ϵ , varies from 1.6 to 2.0 while ϖ_ϵ varies from 0.33 to 0.27 for isotropically-scattering particles (*c.f.*, Figure 9). Thus multiple scattering effects are non-negligible for the ϵ ring periapsis, but may be ignored at the apoapsis.

The fit of the $K=1$ model to the entire ring system is shown in Figure 10. Here, the relative ring system brightness as a function of azimuth angle, ϕ , is calculated as:

$$B(\phi)/B(180^\circ) = P(\phi) * [\sum W_i(\phi+\delta_i) * I/F_i(\tau_i(\phi+\delta_i)) + W_0 * I/F_0], \quad (5)$$

where $P(\phi)$ is the projection factor for the width of the rings on the sky, $W_i(\phi+\delta_i)$ represents the azimuthally-dependent width of ring i , with $i = \alpha, \beta, \epsilon$; W_0 is the radially-integrated width of the other rings, $I/F_i(\tau_i(\phi+\delta_i))$ is the azimuthally-dependent I/F of the α , β , and ϵ rings, and I/F_0 is the I/F of the remaining rings. The origin of ϕ is due north (on the sky), and δ_i is the azimuthal offset of the i th ring periapsis from this origin: 28, 107, and 183 degrees for the ϵ , α , and β ring, respectively. The projection factor is

$$P(\phi) = (\cos^2(\phi) + \sin^2(\phi)\sin^2(\alpha))^{1/2}, \quad (6)$$

where α is the sub-Earth latitude (here, -51.2°). $W_i(\phi+\delta_i) = W_{i,avg} - D_i \cos(\phi+\delta_i)$, where $W_{i,avg}$ is 57.8, 7.5, and 8.7 km for the ϵ , α , and β ring, respectively, and D_i is 38.0, 3.0, and 3.3 km. The azimuthally-dependent optical depth, $\tau_i(\phi+\delta_i)$, is

$$\begin{aligned} \tau_i(\phi+\delta_i) &= \tau_{i,p} W_i(0)/W_i(\phi+\delta_i) \\ &= \tau_{i,p} [W_{i,avg} - D_i]/[W_{i,avg} - D_i \cos(\phi+\delta_i)]. \end{aligned} \quad (7)$$

W_0 is 20.3 km and I/F_0 is 0.02, so as to yield $K = 1$.

The doubling-adding code was used to evaluate $I/F_\epsilon(\tau_\epsilon(\phi+\delta_\epsilon))$ around the ring, using the previously-derived $K = 1$ model parameters of $\omega_\epsilon = 0.294$ and $\tau_{\epsilon,p} = 1.78$. $I/F_\alpha(\tau_\alpha(\phi+\delta_\alpha))$ and $I/F_\beta(\tau_\beta(\phi+\delta_\beta))$ were also evaluated, scaling $\tau_{\alpha,p}$ and $\tau_{\beta,p}$ to $\tau_{\epsilon,p}$ utilizing the relative visual ring opacities of Svitek and Danielson 1987. In these calculations, the single-scattering albedo for the α and β rings were scaled as well by the relative visual single-scattering albedos derived by Svitek and Danielson 1987. The

resulting modelled azimuthal brightness distribution, normalized to the southern ansa, is shown in Figure 10 compared to the observed K-filter distribution. The fit is adequate, although the observations exceed the model in the eastern sector (on the sky) by more than 10%. This may be due to unusually large scattered light from the south pole of Uranus, which is offset about 1 arc sec to the east from the center-of-disk.

FIGURE 11

Figure 11 shows the azimuthal distribution of τ_ϵ and I/F_ϵ , the opacity and flux from the ϵ ring. Both parameters are generally anti-correlated with the integrated ring brightness shown in Figure 10, showing that the variation in projected width of the ϵ ring is the predominant driver of ring brightness. At periapsis, the intrinsic ϵ ring opacity is approximately five times larger and the I/F is about 50% greater than at apoapsis, but the integrated ring system brightness is about 50% less due to the factor-of-five reduction in the width of the ϵ ring.

Analytically, where multiple scattering is negligible, such as at the ϵ ring apoapsis, I/F_ϵ can be expressed as:

$$I/F_\epsilon = [(P_\epsilon(\alpha) \varpi_\epsilon)/4] (\mu_0/(\mu + \mu_0)) \{1 - \exp[-\tau_\epsilon (1/\mu + 1/\mu_0)]\}. \quad (8)$$

Here, $P_\epsilon(\alpha)$ is the area-weighted average particle phase function (normalized to 4π) at a solar phase angle α , ϖ_ϵ is the area-weighted average particle single-scattering albedo, τ_ϵ is the normal optical depth, and μ and μ_0 are the cosines of the emission and incidence angles, respectively, measured from the ring plane normal (*c.f.* Cuzzi *et al.* 1984; Ockert *et al.* 1987; Svitek and Danielson 1987). At $\alpha = 0$, the first square-

bracketted term in (8) is the spherical geometric albedo of assumed spherically-shaped ϵ ring particles, p_ϵ . From (8) and the derived single-scattering albedo for isotropically-scattering particles, ϖ_ϵ and p_ϵ can be determined for any assumed particle phase function. In Tables III and IV, we show these values for ϵ -ring particle visible phase functions favored by Ockert *et al.* 1987 and Karkoschka 1997, as determined from Voyager and Hubble Space Telescope observations. Specifically, we adopt $P_\epsilon(2.4^\circ)$ values of 8.295 and 9.935 for Ockert *et al.* 1987 and Karkoschka 1997, respectively, and associated $P_\epsilon(0^\circ)$ values of 9.051 and 13.25. We note that in the visible the phase behavior of ring particles and dark asteroids has been found to be similar (*c.f.*, Karkoschka 1997), not surprising considering the large size of each particle: with a mean radius greater than 70 cm (Esposito *et al.* 1991) a typical "particle" incorporates more than a ton (10^6 g) of material for even the lightest (0.69 gm/cm^3) plausible hydrocarbon material.

For the Ockert phase function, $\varpi_\epsilon = 0.036 \pm 0.003$ and $p_\epsilon = 0.080 \pm 0.004$ at $2.2 \text{ } \mu\text{m}$ (*c.f.*, Table III), 130 ± 12 percent greater than values found for the visible by Ockert *et al.* 1987, and 69 ± 9 percent greater than the $0.55\text{-}\mu\text{m}$ values. The Karkoschka phase function yields $\varpi_\epsilon = 0.030 \pm 0.004$ and $p_\epsilon = 0.098 \pm 0.009$. Although the particle single-scattering albedo is smaller than derived from the Ockert phase function, the Karkoschka phase function yields a larger geometric albedo due to the much larger back-scattering peak.

3.4 Satellites

FIGURE 12

FIGURE 13

The measured near-infrared satellite full-disk albedos are listed in Table V and displayed in Figures 7, 12, and 13. Throughout the measured spectral range, Ariel, with a full-disk albedo of ~ 0.4 , is 50-100% brighter than either Miranda and Titania. Unlike the other satellites and the ring system, Miranda is less reflective in the near-infrared near-continuum (e.g. H' band) than in the visible (*c.f.*, Figure 7), suggesting a distinctive difference in the bulk distribution of surface materials. Water ice absorption, well-documented for all three satellites in the relative spectroscopic measurements of Cruikshank and Brown 1981, Brown and Cruikshank 1983, and Brown and Clark 1984, is readily detected in the H/H' contrast observed on these bodies. Figure 12 indicates the greatest H/H' water ice absorption band depth occurs for the darkest near-infrared satellite, Miranda, an unexpected result (*c.f.*, Clark and Lucey 1984). Titania exhibits the smallest band depth, more in keeping with its relatively dark albedo compared to Ariel.

FIGURE 14

Miranda is unusual as well in its substantial near-infrared opposition surge, as reported here for both K and H filters between phase angles of 0.6 and 2.4 degrees (*c.f.* Table VI and Figure 14). In K, the magnitude of Miranda increases by 0.1 magnitudes per degree between 2.4 and 1.0 degrees phase, increasing to greater than 0.5 magnitudes per degree between 1.0 and 0.6 degrees phase. This latter measurement significantly exceeds the surge observed between 0.5 and 0.2 degrees phase by Brown and Cruikshank 1983 for Ariel, Oberon, and Titania, and thus indicates the

Table VI

largest near-infrared opposition surge yet measured for the uranian satellites.

4. DISCUSSION

4.1 Ring Composition

Several ring particle optical properties are similar to the material found on the darkside of Iapetus and to the carbonaceous material extracted from the Murchison C2 chondrite. These include the general character of the featureless, near-ir-brightened yet dark broadband spectrum and the low visible spherical particle geometric albedo. Our derived spherical geometric albedo of 0.045-0.050 at 0.55 μm for ϵ ring particles (*c.f.* Table III) is midway between the Cruikshank *et al.* 1983 values of 0.018 for the residue of the Murchison C2 chondrite and the visible geometric albedo of 0.081 ± 0.008 found for the dark hemisphere of Iapetus. These differences could be attributable in part to darkside contamination by relatively-bright polar ices on Iapetus as well as to differences in the microstructure of the satellite and ring particle surfaces. As shown by Johnson and Fanale (1973, Figure 4), particle size is a particularly strong driver of reflectance for the Murchison C2 carbonaceous chondrite, where the reflectance for small particles ($< 0.74 \mu\text{m}$ diameter) is about double that for large particles (147-400 μm).

FIGURE 15

We find a good near-infrared spectral match between our ring spectrum and the absolute reflectance of ~60% clay and ~40% organic mixtures measured by Bell *et al.* 1985. As shown in Figure 15, both the

absolute reflectance and flat spectral character of the rings matches the processed coal tar extract well from 0.6 to 2.2 μm , except for the 0.9- μm absorption discussed previously. Spectral points in the uv and blue (notably, 0.34 and 0.47 μm) appear somewhat high; however mixture reflectivity is not reported in the uv. The somewhat high 0.47 μm point, as well as the uv-visible spectrum from 0.34-0.73 μm , matches well the pure organic material from the Murchison meteorite (*c.f.* panel b of Figure 8), suggesting that a relevant organic component occurring within the meteoritic material is missing from the processed coal tar/clay mixture. In any case, both the low geometric albedo and near-ir brightened spectral character of the ring data suggests that, like the Murchison extract, the processed coal tar, and the darkside of Iapetus (*c.f.*, Squyres and Sagan 1983; Bell *et al.* 1985; Wilson and Sagan 1995; Wilson and Sagan 1996), the uranian ring surface material is comprised substantially of high stoichiometric ratio C:H material, including various polymorphs of elemental carbon and organic polymers, similar to the carbonaceous phases found in the C chondrites.

The Murchison carbonaceous chondrite extract, the Iapetus dark side spectra, and the Uranus ring spectra all exhibit an absorption near 0.6-0.7 μm (*c.f.*, Figure 8). The detailed structure of this absorption varies, being narrow (less than 0.1 μm wide) and centered at 0.6 μm on Iapetus, broad (more than 0.2 μm wide) in the Murchison extract, and of medium breadth (less than 0.15 μm wide) and centered near 0.67 μm in the uranian rings. A feature similar to the ring feature is found in the small particle spectrum of crushed samples of unaltered (*i.e.*, undissolved) Murchison C2 meteorite material (Johnson and Fanale 1973), indicating that a small silicate mineral

component, as found in undissolved Murchison material, may also be incorporated into the ring. As noted earlier, (Section 3.2), the prominent absorption at 0.9 μm is consistent with pyroxene but not olivine nor high stoichiometric ratio C:H material, indicating an additional refractory component.

Like the darkside of Iapetus, the observed optical properties of uranian ring particles reported here are consistent with the hypothesis that ring particle surfaces are highly-evolved "weathered" forms of the bulk material. In the case of Iapetus, proposed weathering mechanisms include (1) devolitization of the predominant bright surface water ice by impacting debris from Phoebe or other unknown outer satellites, resulting in an enhanced concentration of trace indigenous carbonaceous material in a refractory "lag deposit" (Cruikshank *et al.* 1983), and (2) ion and/or ultraviolet darkening of volatile hydrocarbon-rich clathrate/ice, either (2A) originally darkened near the time of satellite formation, subsequently covered by bright water ice, and recently exhumed by impact erosion (Wilson and Sagan 1996), or (2B) originally segregated as pristine material underneath the water ice but more recently exposed at the surface by impact ablation of debris from Phoebe (Squyres and Sagan 1983). In both 2A and 2B, sunlight and solar wind exposure of the initial mixture of $\text{CH}_4/\text{NH}_3/\text{H}_2\text{O}$ ices and clathrates produces a variety of organic chromophores, including polyaromatic hydrocarbons, porphyrins, and conjugated polyenes (Khare *et al.* 1993), which darken quickly (under a few millennia at Uranus's distance from the Sun, appropriately scaling Wilson and Sagan's 1996 analysis based on Khare *et al.*'s 1993 assessment of the conversion rate of hydrocarbon clathrate to complex organic

material). A related hydrocarbon condensate "tanning" mechanism has also been invoked by Baines and Smith 1990 to explain the apparent rapid darkening of pure hydrocarbon ices photochemically produced within the high stratosphere of Neptune. They suggest that exposure to UV irradiation appreciably darkens the precipitating lower stratospheric ices in under a decade, causing the quasi-correlation of planetary albedo with the solar cycle. Such a UV-induced tanning mechanism could explain the observed dark, featureless spectrum of the uranian ring system as well, although laboratory measurements are needed to confirm the near-infrared spectral brightening observed in the ring spectrum.

For Iapetus, magnetospheric charged particle irradiation is not expected to be a primary weathering mechanism since the satellite lies outside the saturnian magnetosphere. However, residing at just two uranian radii from the planet's center, the rings are well-exposed to hydrocarbon-ice-darkening magnetospheric ions, in addition to the solar wind and uv irradiation. Such a darkening mechanism was first suggested by Cheng and Lanzerotti 1978 immediately upon Sinton's 1977 determination that ring system particles are visually dark. Subsequent laboratory measurements of ion-bombarded methane ice by Calcagno *et al.* 1985 showed that for fluences greater than 10^{17} protons cm^{-2} a high stoichiometric ratio C:H substance is produced. This material exhibits a dark, featureless, near-infrared-brightened spectrum, resembling the IRTF/HST uranian ring spectrum presented here. Such darkening to a depth of 100 μm is expected to occur in 10^3 - 10^4 years, based on Voyager measurements of the radiation environment (Lanzerotti and Johnson 1987).

The spectral results reported here support the picture of a collisionally evolving uranian ring system, a system comprised of material continuously being lost through particle dissipation/collision mechanisms, but being re-supplied by collisions of ~10-km diameter moonlets (*c.f.*, Esposito and Colwell 1989; Esposito *et al.* 1991). Although low stoichiometric ratio C:H condensates and clathrate ices are unstable at Uranus (*c.f.* Lebofsky 1975; Lunine and Stevenson 1985), ultraviolet or ion weathering of moonlet surfaces could transform volatile low C:H components into non-volatile high C:H materials in a manner similar to that proposed for Iapetus by Cruikshank *et al.* 1983. In turn, this coating of non-volatile material would serve to prevent continuous outgassing of volatile light hydrocarbons from the interior, much as has been invoked to suppress the rapid outgassing of volatiles from the interiors of comets. Upon intra-moonlet collisions, the volatile, bright but darkenable hydrocarbon/methane-clathrate ice debris would immediately begin to darken as it was distributed to the rings. Since the time scale for hydrocarbon/clathrate weathering and darkening via magnetospheric particle irradiation ($< 10^4$ years; Lanzerotti and Johnson 1987; Wilson and Sagan 1996, extrapolated to Uranus) is much less than the time scales for ring particle dissipation and replenishment of fresh material ($\sim 10^8$ years; Esposito and Colwell 1979), the weathered ring material appears dark.

4.2 Ring Structure

Table VII

Our full-disk ring albedo and derived ring opacities are similar to previous near-infrared investigations, all of which pertained only to the K band at $2.20 \mu\text{m}$ (*c.f.* Table VII). The full-disk albedo primarily depends

on the ring inclination angle, the phase angle, and the angle of ϵ ring periapse. Our measurement agrees particularly well with the values obtained by Matthews *et al.* 1982 for a similar set of angular values. Some discrepancy likely can be attributed to the variety of techniques used, including multi-aperture photometry (Nicholson and Jones 1980; Matthews *et al.* 1982), spectroscopy (Nicholson *et al.* 1983), and raster scanning (Nicholson 1984) vs the direct imaging utilized in this work.

Our observations of the ring system, acquired over a variety of phase angles, is not inconsistent with the K-band opposition surge observed by Herbst *et al.* 1987. The major surge reported by Herbst occurs at phase angles less than 0.5° , outside our range of observations. Within the 0.6 - 2.5° range common to both investigations, a 0.1 magnitude variability is observed, with a slightly larger variability reported here. This is primarily due to the different inclination angle of our 1995 observations compared to 1985 when the ring plane was nearly perpendicular to the Earth line-of-sight. At an inclination angle of 5° , such as occurred in 1985, the ring system is nearly fully open, and the projected area on the sky of any ring segment, for example the dark ϵ ring periapsis, is nearly independent of the ϵ ring periapse angle. The observed full-disk ring albedo is thus unmodulated by periapse location. In our 40° -inclination observations, however, the full-disk albedo is sensitive to the periapse angle, with the geometric albedo increasing by 7% as the ϵ ring periapsis rotates from a southwestern (on the sky) to western orientation as the phase angle increases from 0.6 to 1.0 degrees.

4.3 Satellites

Our observations show that Miranda exceeds both Ariel and Titania in near-infrared opposition surge, near-infrared surface darkness, and water-ice band depth. The former may be indicative of a more fluffy, compacted surface (Buratti *et al.* 1990), but also is not unexpected for relatively dark surfaces (Veeverka 1977; Brown and Cruikshank 1983) such as observed here. The large water-ice band depth is not expected for mixtures of uniformly distributed low reflectance material imbedded within pure water ice (*c.f.*, Clark and Lucey 1984), indicating that Miranda's surface material may be distributed heterogeneously, with perhaps localized outcroppings of significantly purer water ice.

Comparison of our near-infrared spectra with UV-visible spectra obtained at comparable phase angles during the 1995 opposition from the Hubble Space Telescope (Karkoschka 1997) show that Miranda and Titania are relatively dark (full disk albedo less than 0.34) throughout the 0.34-2.2- μm spectral interval (*c.f.* Figure 7). Ariel - the brightest satellite with an H' full disk albedo of 0.47 ± 0.03 - and Titania show a near-infrared brightening, not inconsistent with the ring spectrum and the darkside of Iapetus. This suggests that perhaps these nominally pure water ice satellite surfaces are contaminated with the same kind of weathered high stoichiometric ratio C:H material that is postulated for the rings. It seems unlikely that the material for both satellites originated from the same moonlet source which supplied the ring material, since darker Titania lies more than nine uranian radii farther from the ring/moonlet system than brighter Ariel. However, Titania's larger size (twice the area and 2.7 times

the mass) and gravitational reign over a much larger realm of space may indeed allow a comparable flux of moonlet debris. However, the substantially weaker magnetosphere at Titania compared to Ariel reduces significantly the ion flux at Titania, and thus argues against the charged-particle flux mechanism as a primary common darkening agent. Also, devolitization of light hydrocarbon debris, both upon collision of the moonlets which created the debris as well as subsequent high-velocity collision with the satellites, is unlikely to allow the debris itself to be the source of darkenable hydrocarbon materials. Instead, as has been postulated for the darkside of Iapetus (Squyres and Sagan 1983), the infall of such debris may serve to garden the water-ice dominated satellite surfaces, allowing underlying hydrocarbon-rich ices and clathrates to be exposed to solar UV-irradiation.

Miranda is the closest satellite to the uranian rings, and is deeply imbedded within the uranian magnetic field, so its (postulated) indigenous hydrocarbon-rich interior should be the most susceptible to surface gardening by moonlet debris and subsequent hydrocarbon weathering. Indeed, its relatively low near-infrared albedo suggests that it has suffered such enhanced darkening processes. However, Miranda's full-disk visible - near-infrared spectral character is inconsistent with that of the rings or Iapetus, being spectrally blue rather than red (*c.f.* Figure 7), more consistent with the general character of pure water ice. This spectral behavior may be an additional indication, beyond the enhanced water band depth discussed earlier, that Miranda's surface material may be distributed heterogeneously, with perhaps localized outcroppings of significantly purer water ice. If so, then Miranda's dark material - like that

of the rings - may indeed be consistent with ion/uv-induced weathering of indigenous light hydrocarbons.

ACKNOWLEDGMENTS

The authors would like to thank Robert H. Brown and Bonnie Buratti for helpful discussions pertaining to the surfaces of the uranian satellites. This work also benefitted tremendously from frank and useful discussions with Carl Sagan during his last visit to JPL in December, 1995. We would also like to thank Will Grundy and an anonymous referee for useful comments and suggestions. The work described in this paper was carried out by the Jet Propulsion Laboratory, Pasadena, California, under contract with the National Aeronautics and Space Administration, with support from the Planetary Astronomy and Planetary Atmospheres Disciplines, NASA Office of Space Sciences and Applications. Observations were conducted at the NASA/Infrared Telescope Facility, Mauna Kea, Hawaii.

REFERENCES

Arvesen, J. C., R. N. Griffin, Jr., and B. D. Pearson, Jr. 1969. Determination of extraterrestrial solar spectral irradiance from a research aircraft. *Appl. Opt.* **8**, 2215-2232.

Baines, K. H. and J. T. Bergstralh 1986. The structure of the uranian atmosphere: Constraints from the geometric albedo spectrum and H₂ and CH₄ line profiles. *Icarus* **65**, 406 - 411.

Baines, K. H. and H. B. Hammel 1994. Clouds, hazes, and the stratospheric methane abundance in Neptune. *Icarus* **109**, 20 - 39.

Baines, K. H. and W. H. Smith 1990. The atmospheric structure and dynamical properties of Neptune derived from ground-based and IUE spectrophotometry. *Icarus* **85**, 65 - 108.

Baines, K. H., M. E. Mickelson, L. E. Larson, and D. W. Ferguson 1995. The abundances of methane and *ortho/para* hydrogen on Uranus and Neptune: Implications of new laboratory 4-0 H₂ quadrupole line parameters. *Icarus* **114**, 328-340.

Baines, K. H., R. A. West, L. P. Giver, and F. Moreno 1993. Quasi-random narrow band model fits to near-infrared low-temperature laboratory methane spectra and derived exponential-sum absorption coefficients. *J. Geophys. Res. - Planets* **98**, E3, 5517-5529.

Bell, J. F., D. P. Cruikshank, and M. J. Gaffey 1985. The composition and origin of the Iapetus dark material. *Icarus* **61**, 192-207.

Bergstralh, J. T., G. S. Orton, D. J. Diner, K. H. Baines, J. S. Neff, and M. A. Allen 1981. Spatially resolved absolute spectrophotometry of Saturn: 3390 to 8080 Å. *Icarus* **46**, 27 - 29.

Binzel, R. P., S. M. Slivan, P. Magnusson, W. Z. Wisniewski, J. Drummond, K. Lumme, M. A. Barucci, E. Dotto, C. Angeli, D. Lazzaro, S. Mottola, M. Gonano-Beurer, T. Michalowski, G. De Angelis, W. J. Wild, D. J. Tholen, M. DiMartino, M. Hoffmann, E. H. Geyer, and F. Veluchko 1993. Asteroid Ida: Groundbased photometry and a pre-Galileo physical model. *Icarus* **105**, 310-325.

Bodenheimer, P., and J. B. Pollack 1986. Calculations of the accretion and evolution of giant planets: The effects of solid cores. *Icarus* **67**, 391-408.

Brown, R. H. 1983. The uranian satellites and Hyperion: New spectrophotometry and compositional implications. *Icarus* **56**, 414-425.

Brown, R. H. and R. N. Clark 1984. Surface of Miranda: Identification of water ice. *Icarus* **58**, 288 - 292.

Brown, R. H., and D. P. Cruikshank 1983. The uranian satellites: Surface compositions and opposition brightness surges. *Icarus* **55**, 83-92.

Brown, R. H., T. V. Johnson, S. Synott, J. D. Anderson, R. A. Jacobson, S. F. Dermott, and P. C. Thomas 1991. Physical properties of the uranian satellites. In *Uranus* (J. T. Bergstralh, E. D. Miner, and M. S. Matthews, Eds),. pp. 513-527. Univ.of Arizona Press, Tucson.

Buratti, B., F. Wong, and J. Mosher 1990. Surface properties and photometry of the uranian satellites. *Icarus* 84, 203 - 214.

Calcagno, L., G. Foti, L. Torrisi, and G. Strazzulla 1985. Fluffy layers obtained by ion bombardment of frozen methane: Experiments and applications to Saturn and and uranian satellites. *Icarus* 63, 31 - 38.

Cheng, A. F., and L. J. Lanzerotti 1978. Ice sputtering by radiation belt protons and the rings of Saturn and Uranus. *J. Geophys. Res.* 83, 2597-2602.

Clark, R. N. and P. G. Lucey 1984. Spectral properties of ice-particulate mixtures and implications for remote sensing 1. Intimate mixtures. *J. Geophys. Res.* 89, 6341-6348.

Cloutis, E. A. 1989. Spectral reflectance properties of hydrocarbons: Remote-sensing implications. *Science* 245, 165-168.

Cruikshank, D. P., and R. H. Brown 1981. The uranian satellites: Water ice on Ariel and Umbriel. *Icarus* 45, 607-611.

Cruikshank, D. P., J. F. Bell, M. J. Gaffey, R. H. Brown, R. Howell, C. Beerman, and M. Rognstad 1983. The dark side of Iapetus. *Icarus* **53**, 90-104.

Cuzzi, J. N., J. L. Lissauer, W. Esposito, J. B. Holberg, E. A. Marouf, G. L. Tyler, and A. Boischot 1984. Saturn's rings: Properties and processes. In *Planetary Rings* (R. Greenberg and A. Brahic, Eds), pp. 73-199. Univ. of Arizona Press, Tucson.

Esposito, L. W. and J. E. Colwell 1989. Creation of the Uranus rings and dust bands. *Nature* **339**, 605 - 607.

Esposito, L. W., A. Brahic, J. A. Burns, and E. A. Marouf. 1991. Particle properties and processes in Uranus' rings. In *Uranus* (J. T. Bergstralh, E. D. Miner, M. S. Matthews, Eds.), pp. 410-465. Univ of Arizona Press, Tucson.

French, R. G., P. D. Nicholson, C. C. Porco, and E. A. Marouf 1991. Dynamics and structure of the uranian rings. In *Uranus* (J. T. Bergstralh, E. D. Miner, and M. S. Matthews, Eds.), pp. 327-409. Univ. of Arizona Press, Tucson.

Guarnieri, M. D., R. I. Dixon, and A. J. Longmore 1991. The accuracy of infrared photometry with arrays. *Publ. Astron. Soc. Pac.* **103**, 675-684.

Hammel, H. B., K. H. Baines, and J. T. Bergstralh 1989. Vertical aerosol structure of Neptune: Constraints from center-to-limb profiles. *Icarus* **80**, 416-438.

Helfenstein, P., J. Veverka, P. C. Thomas, D. P. Simonelli, K. Klaasen, T. V. Johnson, F. Fanale, J. Granahan, A. S. McEwen, M. Belton, and C. Chapman 1996. Galileo photometry of asteroid 243 Ida. *Icarus* **120**, 48-65.

Herbst, T. M., M. F. Skrutskie, and P. D. Nicholson 1987. The near-infrared phase curve of the uranian rings. *Icarus* **71**, 103-114.

Johnson, V. T. and F. P. Fanale 1973. Optical properties of carbonaceous chondrites and their relationship to asteroids. *J. Geophys. Res.* **78**, 8507 - 8518.

Karkoschka, E. 1997. Rings and satellites of Uranus: Colorful and not so dark. *Icarus* **125**, 348-363.

Khare, B. N., W. R. Thompson, L. Cheng, C. F. Chyba, C. Sagan, E. T. Arakawa, C. Meisse, and P. S. Tuminello 1993. Production and optical constants of ice tholin from charged particle irradiation of (1:6) C₂H₆/H₂O at 77 K. *Icarus* **103**, 290-300.

Lanzerotti, L. J. and R. E. Johnson 1987. Astrophysical implications of ions incident on insulators. In *Ion Beam Modification of Insulating Materials*. (P. Mazzoldi and G. W. Arnold, Eds). Elsevier, New York.

Lebofsky, L. A. 1975. Stability of frosts in the Solar System. *Icarus* **25**, 205-217.

Lunine, J. I. and D. J. Stevenson 1985. Thermodynamics of clathrate hydrate at low and high pressures with applications to the outer Solar System. *Astrophys. J. Suppl.* **58**, 493 - 531.

Matthews, K., G. Neugebauer, and P. D. Nicholson 1982. Maps of the rings of Uranus at a wavelength of 2.2 microns. *Icarus* **52**, 126-135.

Nautical Almanac 1995. pp F63-F66.

Nicholson, P. D. 1984. Infrared images of the uranian rings. In *Uranus and Neptune*. (J.T. Bergstralh, Ed). NASA CP 2330, pp 589-608.

Nicholson, P. D. and T. J. Jones 1980. Two-micron spectrophotometry of Uranus and its rings. *Icarus* **42**, 54-67.

Nicholson, P. D., T. J. Jones, and K. Matthews 1983. Infrared observations of the uranian rings. In *Planetary Rings*. (A. Brahic, Ed.) I.A.U. Colloquim No. 75.

Ockert, M. E., J. N. Cuzzi, C. C. Porco, and T. V. Johnson 1987. Uranian ring photometry: Results from Voyager 2. *J. Geophys. Res* **92**, 14969-14978.

Pollack, J. B., M. Podolak, P. Bodenheimer, and H. Christofferson 1986. Planetesimal dissolution in the envelopes of the forming giant planets. *Icarus* **67**, 409-443.

Porco, C. C., J. N. Cuzzi, M. E. Ockert, and R. J. Terrile 1987. The color of the uranian rings. *Icarus* **72**, 69-78.

Schmitt, B., E. Quirico, and E. Lellouch 1993. Near infrared spectra of potential solids at the surface of Titan. In *Symposium on Titan*, Conference Proceedings, ESA SP-338, pp 383-388.

Sinton, W. M. 1977. Uranus: The rings are black. *Science* **198**, 503 - 504.

Smith, B. A., L. A. Soderblom, R. Beebe, D. Bliss, J. M. Boyce, J. M. Brahic, G. A. Briggs, R. H. Brown, S. A. Collins, A. F. Cook II, S. K. Croft, J. N. Cuzzi, G. E. Danielson, A. P. Ingersoll, T. V. Johnson, R. J. Krauss, H. Masursky, D. Morrison, T. Owen, J. B. Plescia, J. B. Pollack, C. C. Porco, K. Rages, C. Sagan, E. M. Shoemaker, L. A. Sromovsky, C. Stoker, R. G. Strom, V. E. Suomi, S. P. Synnott, R. J. Terrile, P. Thomas, W. R. Thompson, and J. Veverka 1986. Voyager 2 in the uranian system: Imaging science results. *Science* **233**, 43-64.

Squyres, S. W. and C. Sagan 1983. Albedo asymmetry of Iapetus. *Nature* **303**, 782 - 785.

Svitek, T. and G. E. Danielson 1987. Azimuthal brightness variation and albedo measurements of the uranian rings. *J. Geophys. Res.* **92**, 14979-14986.

Tholen, D. J. 1994. Unpublished data included in Fig. 1 of Helfenstein *et al.* 1996. *Icarus* **120**, p. 53.

Wilson, P. D. and C. Sagan 1995. Spectrophotometry and organic matter on Iapetus. I. Composition models. *J. Geophys. Res.- Planets* **100**, 7531-7537.

Wilson, P. D. and C. Sagan 1996. Spectrophotometry and organic matter on Iapetus. 2. Models of interhemispheric asymmetry. *Icarus* **122**, 92-106.

Veverka, J. 1977. Photometry of satellite surfaces. In *Planetary Satellites* (J. A. Burns, Ed.), pp. 171-231. Univ. of Arizona Press, Tucson.

Zellner, B., D. J. Tholen, and E. F. Tedesco 1985. The eight-color asteroid survey: Results for 589 minor planets. *Icarus* **61**, 335-416.

Table I
Log of Observations

| Object | Time | Total | Filter | Air- | PSF FWHM** |
|--------|------|-------------|--------|------|------------|
| | (UT) | Integration | Name* | Mass | (arc-sec) |
| | | Time | | | E-W N-S |
| | | (Sec) | | | |

July 10, 1995

Phase angle: 0.6 degrees

| | | | | | |
|--------|-------|-----|---|-------|-----------|
| Uranus | 13:16 | 20 | H | 1.571 | 0.82 0.87 |
| System | 13:17 | 400 | K | 1.595 | |

August 10, 1995

Phase Angle: 1.0 degrees

| | | | | | |
|--------|-------|------|----|-------|--|
| UKFS34 | 08:54 | 10.0 | J | 1.352 | |
| | 08:54 | 50.0 | H | 1.350 | |
| | 08:57 | 50.0 | H' | 1.347 | |
| | 08:59 | 50.0 | K | 1.344 | |

Table I (Continued)

| | | | | | | |
|--------|-------|------|----|-------|------|------|
| Uranus | 09:12 | 40.0 | J | 1.325 | | |
| System | 09:14 | 40.0 | H | 1.326 | 0.86 | 0.88 |
| | 09:16 | 200 | H' | 1.326 | | |
| | 09:23 | 600 | K | 1.329 | | |
| UKFS34 | 10:13 | 10.0 | J | 1.310 | | |
| | 10:15 | 50.0 | H | 1.312 | | |
| | 10:16 | 50.0 | H' | 1.313 | | |
| | 10:17 | 50.0 | K | 1.315 | | |
| UKFS34 | 11:26 | 10.0 | J | 1.447 | | |
| | 11:26 | 50.0 | H | 1.448 | | |
| | 11:27 | 50.0 | H' | 1.452 | | |
| | 11:30 | 50.0 | K | 1.459 | | |
| UKFS34 | 11:57 | 10.0 | J | 1.570 | | |
| | 11:57 | 50.0 | H | 1.575 | | |
| | 11:59 | 50.0 | H' | 1.584 | | |
| | 12:02 | 50.0 | K | 1.600 | | |

Table I (Continued)

September 16, 1995

Phase angle: 2.4 degrees

| | | | | | | |
|--------|-------|------|----|-------|------|------|
| UKFS34 | 08:15 | 10.0 | J | 1.347 | | |
| | 08:16 | 50.0 | H | 1.347 | | |
| | 08:18 | 50.0 | H' | 1.348 | | |
| | 08:21 | 50.0 | K | 1.349 | | |
| Uranus | 08:27 | 40.0 | J | 1.531 | 0.58 | 0.57 |
| System | 08:29 | 40.0 | H | 1.532 | 0.52 | 0.60 |
| | 08:32 | 200 | H' | 1.533 | 0.57 | 0.69 |
| | 08:39 | 400 | K | 1.537 | 0.53 | 0.82 |
| UKFS34 | 08:56 | 10.0 | J | 1.430 | | |
| | 08:57 | 20.0 | H | 1.431 | | |
| | 08:59 | 50.0 | H' | 1.432 | | |
| | 09:02 | 50.0 | K | 1.434 | | |

* Filter effective wavelengths and full-widths half-maxima:

J: 1.27 μm , 0.30 μm ; K: 1.62 μm , 0.28 μm ;

H': 1.73 μm , 0.10 μm ; K: 2.20 μm , 0.39 μm

** Measured platescale: 0.1478 \pm 0.0010 arc-sec/pixel

Table II

Southern and Northern Ring Ansa I/F (Area Corrected)

| Filter | Effective Wave- length (μm) | I/F South | North | South/North I/F Ratio |
|--------|---|---------------------|---------------------|--------------------------|
| J | 1.27 | 0.0281 ± 0.0031 | 0.0299 ± 0.0076 | 0.940 ± 0.273 |
| H | 1.62 | 0.0268 ± 0.0024 | 0.0379 ± 0.0051 | 0.707 ± 0.144 |
| H' | 1.73 | 0.0280 ± 0.0012 | 0.0319 ± 0.0022 | 0.878 ± 0.071 |
| K | 2.20 | 0.0273 ± 0.0008 | 0.0318 ± 0.0016 | 0.858 ± 0.035 |
| Mean | | 0.0275 ± 0.0007 | 0.0322 ± 0.0012 | 0.857 ± 0.030 |

Table III
Visible-Near-Infrared Ring Albedo Characteristics

| Wavelength (μm) | $p(1^\circ)^*$ | ω_ϵ^{**} | p_ϵ^{***} |
|---------------------------------|---------------------|------------------------|---------------------|
| 0.34 | 0.0184 ± 0.0009 | 0.0175 ± 0.0009 | 0.0398 ± 0.0020 |
| 0.47 | 0.0213 ± 0.0011 | 0.0203 ± 0.0010 | 0.0460 ± 0.0023 |
| 0.55 | 0.0222 ± 0.0011 | 0.0211 ± 0.0011 | 0.0479 ± 0.0024 |
| 0.62 | 0.0232 ± 0.0012 | 0.0221 ± 0.0011 | 0.0492 ± 0.0025 |
| 0.67 | 0.0231 ± 0.0012 | 0.0220 ± 0.0011 | 0.0499 ± 0.0025 |
| 0.73 | 0.0247 ± 0.0012 | 0.0236 ± 0.0012 | 0.0533 ± 0.0027 |
| 0.91 | 0.0252 ± 0.0013 | 0.0241 ± 0.0012 | 0.0544 ± 0.0027 |
| 1.27 | 0.0336 ± 0.0042 | 0.0349 ± 0.0043 | 0.0788 ± 0.0099 |
| 1.62 | 0.0320 ± 0.0033 | 0.0332 ± 0.0042 | 0.0752 ± 0.0096 |
| 1.73 | 0.0335 ± 0.0022 | 0.0348 ± 0.0023 | 0.0787 ± 0.0038 |
| 2.20 | 0.0326 ± 0.0015 | 0.0355 ± 0.0016 | 0.0802 ± 0.0038 |

* Full-disk albedo data for $\lambda < 1.0 \mu\text{m}$ from Karkoschka 1997, normalized to ring system area of $2.295 \times 10^6 \text{ km}^2$

** Single-scattering albedo for the ϵ ring derived from 2.2- μm modelled value for 2.4° phase angle, scaled by $p(1^\circ)$

*** ϵ ring particle spherical geometric albedo derived from 2.2- μm modelled value for Ockert *et al.* 1987 phase function, scaled by $p(1^\circ)$

Table IV
Modelled 2.2- μ m Ring Properties

| K | Γ | $\tau_{\epsilon,p}$ | $\tau_{\epsilon,a}$ | $\overline{\omega}_{\epsilon}$ iso | $\overline{\omega}_{\epsilon}$ ock | $\overline{\omega}_{\epsilon}$ kar | P_{ϵ} iso | P_{ϵ} ock | P_{ϵ} kar |
|-----|----------|---------------------|---------------------|---------------------------------------|---------------------------------------|---------------------------------------|-----------------------|-----------------------|-----------------------|
| 0.0 | 0.000 | 1.101 | 0.229 | 0.550 | 0.066 | 0.055 | 0.137 | 0.150 | 0.183 |
| 0.1 | 0.050 | 1.137 | 0.237 | 0.513 | 0.062 | 0.052 | 0.128 | 0.140 | 0.171 |
| 0.2 | 0.102 | 1.255 | 0.262 | 0.460 | 0.056 | 0.046 | 0.115 | 0.126 | 0.151 |
| 0.4 | 0.177 | 1.319 | 0.275 | 0.412 | 0.048 | 0.040 | 0.100 | 0.109 | 0.133 |
| 0.6 | 0.231 | 1.464 | 0.305 | 0.363 | 0.044 | 0.037 | 0.091 | 0.099 | 0.121 |
| 0.8 | 0.273 | 1.622 | 0.338 | 0.327 | 0.039 | 0.033 | 0.082 | 0.089 | 0.109 |
| 1.0 | 0.308 | 1.775 | 0.370 | 0.294 | 0.036 | 0.030 | 0.074 | 0.080 | 0.098 |
| 1.2 | 0.335 | 2.029 | 0.423 | 0.268 | 0.032 | 0.027 | 0.067 | 0.073 | 0.089 |

K: Fraction of ring brightness due to non- ϵ rings within the bright northern ansa on September 16, 1995; true anomaly 28 degrees

Γ : Fraction of ring brightness due to non- ϵ rings within the bright southern ansa on September 16, 1995; true anomaly 208 degrees

$\tau_{\epsilon,p}$: Opacity of ϵ ring at periapsis

$\tau_{\epsilon,a}$: Opacity of ϵ ring at apoapsis

$\overline{\omega}_{\epsilon,iso}$: single-scattering albedo for isotropically-scattering particles

$\overline{\omega}_{\epsilon,ock}$: single-scattering albedo for Ockert *et al.* 1987 ring particle phase function

$\overline{\omega}_{\epsilon,kar}$: single-scattering albedo for Karkoschka 1997 ring particle phase function

$P_{\epsilon,iso}$: spherical geometric particle albedo for isotropically-scattering particles

$P_{\epsilon,ock}$: spherical geometric particle albedo for Ockert *et al.* 1987 particle phase function

$P_{\epsilon,kar}$: spherical geometric particle albedo for Karkoschka 1997 particle phase function

Table V

Full-Disk Albedos

| Object | Phase Angle | Effective Wavelength (μm)/Filter | | | |
|---------|-------------|---|---------------------|-----------------------|-------------------------|
| | | 1.27 J | 1.62 H | 1.73 H' | 2.20 K |
| Uranus | 1.0/2.4 | 0.0190 ± 0.0010 | 0.0200 ± 0.0060 | 0.00146 ± 0.00007 | 0.000114 ± 0.000003 |
| Rings | 1.0 | 0.0336 ± 0.0042 | 0.0320 ± 0.0033 | 0.0335 ± 0.0022 | 0.0326 ± 0.0015 |
| Miranda | 2.4 | 0.217 ± 0.015 | 0.197 ± 0.009 | 0.273 ± 0.008 | 0.220 ± 0.007 |
| Ariel | 1.0 | 0.356 ± 0.025 | 0.347 ± 0.025 | 0.468 ± 0.025 | 0.320 ± 0.016 |
| Titania | 2.4 | 0.253 ± 0.013 | 0.237 ± 0.007 | 0.297 ± 0.008 | 0.239 ± 0.007 |

Table VI

Miranda: Full-Disk Albedo for Various Phase Angles

| Phase Angle (Deg.) | Date Filter | Full-Disk Albedo |
|--------------------|-------------|-------------------|
| 0.6 | 7/10 H | 0.272 ± 0.030 |
| | K | 0.439 ± 0.128 |
| 1.0 | 8/10 K | 0.248 ± 0.010 |
| 2.4 | 9/16 H | 0.197 ± 0.009 |
| | K | 0.220 ± 0.007 |

Table VII

K-Filter Ring System Full-Disk Albedo

| Reference | Inclination Angle (Degrees) | Phase Angle (Degrees) | ϵ Ring Periapse (Degrees) | Full-Disk Albedo |
|------------------------------|--------------------------------|--------------------------|---------------------------------------|---------------------|
| This Work | 40.2 | 0.6 | 233 | 0.0306 ± 0.0020 |
| | 39.1 | 1.0 | 274 | 0.0326 ± 0.0015 |
| | 38.1 | 2.4 | 332 | 0.0309 ± 0.0015 |
| Matthews <i>et al.</i> 1982 | 34.2 | 0.8 | 6 | 0.032 ± 0.005 |
| | 31.1 | 2.6 | 206 | |
| Nicholson and Jones 1980 | 28.3 | 1.1 | 89 | 0.028 ± 0.007 |
| Nicholson <i>et al.</i> 1983 | 16-19.3 | various | various | 0.023 ± 0.002 |
| Nicholson 1984 | 11.2 | 2.7 | 256 | 0.022 ± 0.002 |
| | 12.7 | 0.1 | 339 | |
| | 14.3 | 2.6 | 62 | |
| Herbst <i>et al.</i> 1987 | 5.0 | 0.02 | 268 | 0.0400 ± 0.0025 |
| | | 1.2 | 235 | 0.0298 ± 0.0032 |
| | | 2.5 | 313 | 0.0267 ± 0.0024 |

Column 3 is the inclination of the plane of the rings to the plane of the sky

Column 4 is the position angle of the ϵ ring periapse, measured
counterclockwise from North on the sky.

Figure Captions

Figure 1. Near-infrared high-spatial-resolution ($\text{FWHM} < 0.6$) broadband images of Uranus and its ring system, acquired Sept 16, 1995 with NSFCAM at the NASA/IRTF. Celestial north is at the top, west on the right (*c.f.*, Figure 2). Tropospheric aerosols are observed over the planet's south pole in J and H filter images. Stratospheric aerosols are sampled in H' and K images sensitive to atmospheric methane absorption. Nearly uniform limb brightening suggests a globally uniform stratospheric aerosol distribution. The ring brightness has been enhanced a factor of 100 relative to the planet in J and H images to reveal the ring system against the bright glow of Uranus, the scattered light of which can be seen overlying the eastern and western sections of the ring system in these images. For the H' image, the ring brightness is enhanced by a factor of 5. No enhancement is used for the K image, where the rings naturally outshine the planet. Asymmetrical ring structure is observed particularly well in H' and K imagery, which are largely unaffected by scattered light from the planet. In all images, the southern ring ansa is observed particularly well, located close to the bright apoapsis of the ϵ ring.

Figure 2. Orientation of Uranus and its ring system, September 16, 1995. Celestial north is at the top, west to the right. Sub-Earth latitude is 51.9 degrees South. The planet's South Pole is to the left of center. The full-width-half-maximum of the image point-spread function, measured using a star image observed in the K filter, is shown. The southern ansa, located just 28 degrees longitudinally from the bright ϵ ring apoapsis, is

particularly well-suited for measuring the near-infrared broadband ring spectrum.

Figure 3. Observed mean radial profiles through the southern ring ansa, September 16, 1995. Five neighboring north-south oriented columns centered on the southern ring ansa were used to obtain the average profiles displayed here. Profiles peak near 3.5 arc-secs from the center of Uranus.

Figure 4. Precession of the ϵ ring. K-filter images acquired on (a) July 10, 1995, (b) August 10, 1995, and (c) September 16, 1995 show the bright apoapsis and dark periapsis of ϵ ring precessing 93 degrees about the polar axis during this period, the fastest natural precession ever imaged off the Earth. The true anomaly of the ϵ ring determined for September 16, 1995 is 208 degrees as determined from these images.

Figure 5. Observed photometrically-calibrated central meridian profiles for Uranus, September 16, 1995. Measured uncertainties (not shown) are less than the sizes of the symbols. The deep-absorption H' and K bands show symmetrical profiles, indicating a globally uniform haze distribution in the stratosphere/upper troposphere (above approximately the 200-mbar level). This contrasts with the near-continuum H and J profiles which show an asymmetry peaking near the South Pole, indicating a polar cap of enhanced tropospheric (~1 bar level) cloud material. The measured east-west point-spread function (0.52 arc-sec FWHM) is also shown.

Figure 6. Reduced mean radial profiles through the northern and southern ring ansae, September 16, 1995. Profiles are corrected for scattered light from Uranus as determined from the western profiles. J, H, and H' data are also corrected for uranian scattered light from the secondary mirror support structure ("spider"), as discussed in the text. Error bars show the total composite uncertainty attributable primarily to scattered light and statistical photon uncertainties.

Figure 7. Full-disk absolute albedo spectra of Miranda, Ariel, Titania, and the ring system of Uranus, 0.34 - 2.2 μm . The HST results of Karkoschka 1997 are shown for optical wavelengths shortward of 1.0 μm . (Here, the Karkoschka 1997 Table I full-disk ring albedo values were adjusted to the ring-integrated projected area of $2.30 \times 10^7 \text{ km}^2$ used for 1° phase angle observations in this work). Near-ir bandpasses and filter names are depicted at the bottom. The ring system (bottom spectrum) is 50% brighter in the near-infrared than in the visible. For the satellites Miranda and Titania, observed spectra (solid) and spectra adjusted to 1.0° phase angle (dashed) are shown to facilitate comparison with the 1.0° phase angle HST observations. (For Miranda, values for J, H, and H' were scaled from their 2.4° values utilizing the observed K-band behavior. For Titania, the reflectivity at all wavelengths was adjusted from their 2.4° values using the low-phase-angle brightening reported by Brown and Cruikshank 1983). Over the entire spectral range, Ariel is the brightest of the three satellites. Longward of 0.75 μm , its albedo exceeds that of the other satellites by more than 20%. In the near-infrared, the albedo of Titania exceeds that of Miranda, in contrast to the visible.

Figure 8. Spectrum of the Uranus ring system (open circles and large triangles with error bars) compared to spectra of (A) the darkside of Iapetus, (B) carbonaceous residue of the Murchison meteorite, and (C) Ida. Data is normalized (left-hand scale) to the observed flux at 0.56 μm for the ring system and 0.55 μm for Iapetus, Murchison, and Ida. Right-hand scale shows the full-disk ring-system albedo. All objects are about 50% brighter in the near-infrared than in the visible. In the near-infrared, the ring spectrum is flat, consistent with the Iapetus and Murchison spectra, but inconsistent with the olivine-rich Ida spectrum. From 0.7 to 0.9 μm , the Uranus ring system spectrum is flatter than either Iapetus or Murchison, while from 0.9 to 1.2 μm , the ring spectrum rises much more steeply. This behavior is somewhat consistent with the asteroidal spectrum, and perhaps indicates pyroxene as a ring constituent. Ring system data for wavelengths less than 1.0 μm from Karkoschka 1997; Iapetus and Murchison data from Cruikshank *et al.* 1983; Ida data from Helfenstein *et al.* 1996.

Figure 9. Modelled K-filter single-scattering albedo ($\bar{\omega}_\epsilon$, dashed curve) and optical depth (τ_ϵ , solid curves) for the ϵ ring as a function of K and Γ , defined respectively as the ratio of non- ϵ -ring to ϵ -ring brightnesses at the northern ansa (K , true anomaly 28°) and at the southern ansae (Γ , true anomaly 208°). Periapse optical depth (upper solid) of isotropically-scattering modelled ϵ ring particles varies over nearly a factor of two as K and Γ vary, respectively, from 0.0-1.2 and 0.0 - 0.335.

Figure 10. Uranian ring system brightness $K=1.0$ model vs observations. K-filter brightness relative to southern ansa brightness is shown as a function of relative longitude and true anomaly.

Figure 11. Modeled K-filter I/F and particle opacity for the ϵ ring. I/F (solid) and optical depth (long dashed) are shown as a function of true anomaly for the $K=1.0$ model. As shown on the lower right-hand scale, ϵ -ring opacity varies from 0.37 at apoapsis to 1.78 at periapsis. The full ring system I/F is also shown (short dashed), as are the observed and modelled full-disk albedos for the ring system.

Figure 12. Near-infrared broadband relative spectra of Miranda, Ariel, and Titania. Near-ir bandpasses and filter names are depicted at the bottom. The three satellites exhibit a common H'-K color, to within the measurement uncertainty. Color differences in the J-H-H' region (1.27 - 1.73 μm) are apparent, indicating that Miranda is slightly "redder" in the near-infrared than Titania, consistent with greater water ice absorption on Miranda.

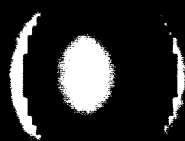
Figure 13. Near-infrared absolute spectrophotometry of the uranian system, September 16, 1995. Full-disk results are shown for Uranus, its ring system, and three satellites - Titania, Ariel, and Miranda. Near-ir bandpasses and filter names are depicted at the bottom. Throughout the near-infrared, methane-darkened Uranus (here displayed with its flux enhanced by a factor of ten) exhibits the darkest full-disk albedo within the uranian system. The ring system is spectrally flat. For the satellites the maximum reflectivity is observed in the C-H absorption band at 1.73 μm ,

indicating that hydrocarbons are not dominant surface constituents. All three satellites are darker at 1.63 μm than at 1.27 and 1.73 μm , consistent with surface water ice absorption. Ariel, observed at 1° phase angle, is some 50% brighter than Titania and Miranda, observed at 2.4° phase angle. Uranus displays an order-of-magnitude drop in full-disk albedo between 1.62 and 1.73 μm , indicative of atmospheric methane absorption.

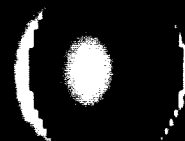
Figure 14. Near-infrared opposition brightness surge of Miranda. K filter (filled circles) and H filter (open triangles) both show a significant increase in albedo as the phase angle is decreased from 2.4 to 0.6° . As for the other major uranian satellites (*c.f.* Brown and Cruikshank 1983), such a brightness surge near opposition is consistent with the relatively dark surfaces observed here.

Figure 15. Ring spectrum compared to spectra of various mixtures of clay and simulated meteorite organics obtained by Bell *et al.* 1985. Both the absolute reflectance and relatively flat shape of the ring spectrum are consistent with a ~40% organic mixture.

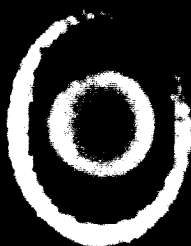
Uranus
NASA/IRTF NSFCAM Images
September 1995



J
 $1.26 \mu\text{m}$



H
 $1.62 \mu\text{m}$



H'
 $1.73 \mu\text{m}$



K
 $2.21 \mu\text{m}$

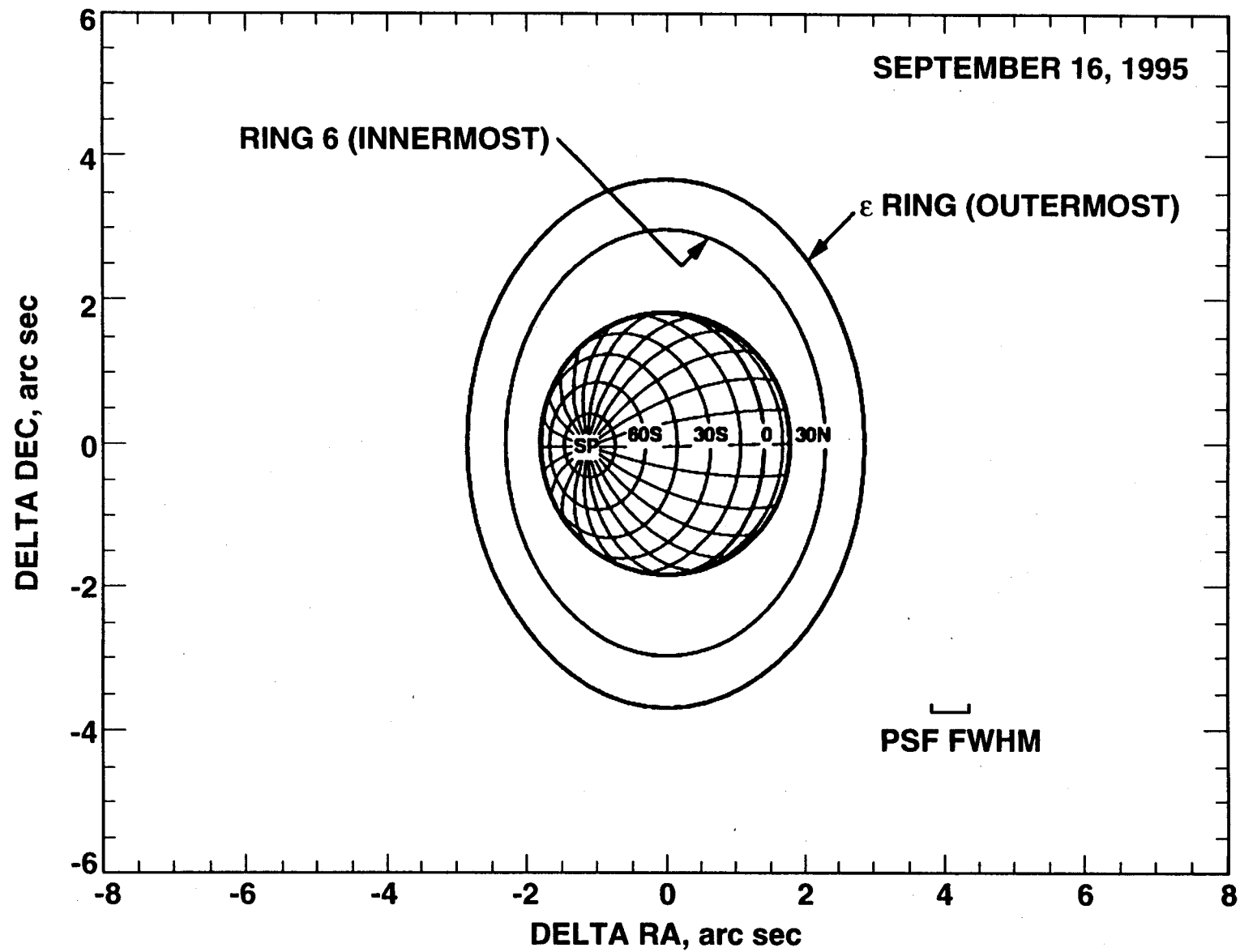
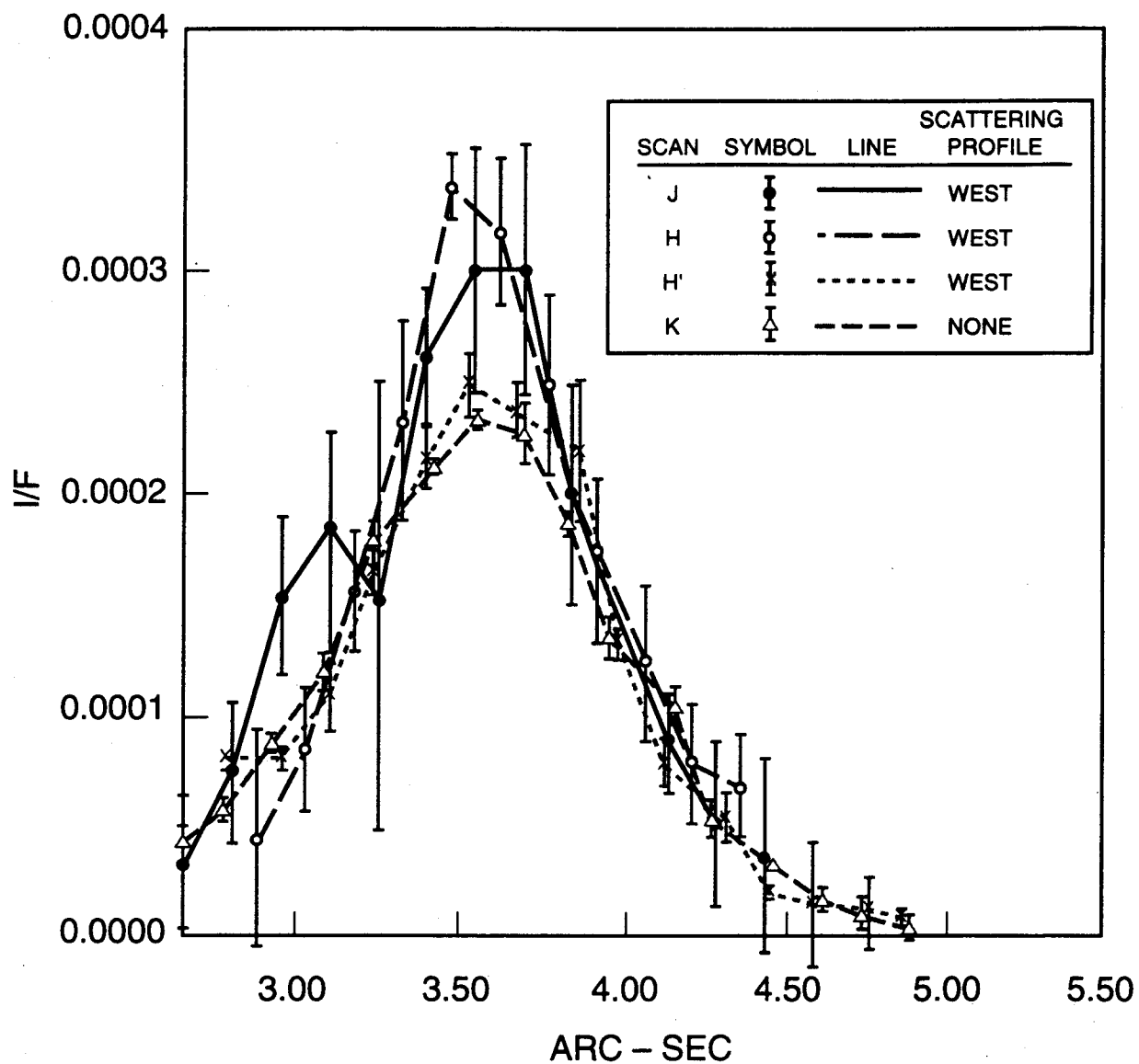


FIGURE 2

FIGURE 3



Uranus
Near-Infrared Images
Precession of the Epsilon-Ring



K
July 1995



K
August 1995



K
September 1995

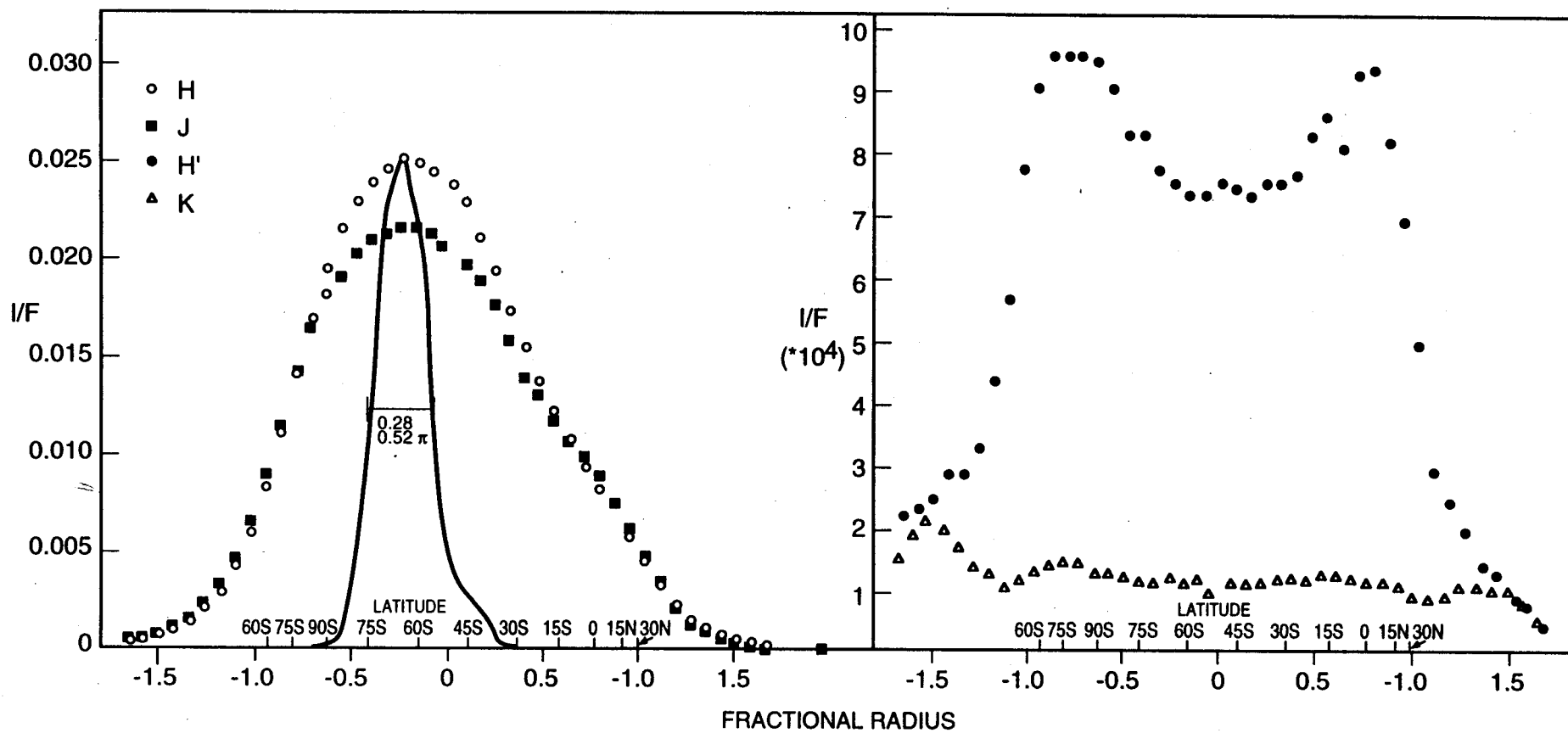
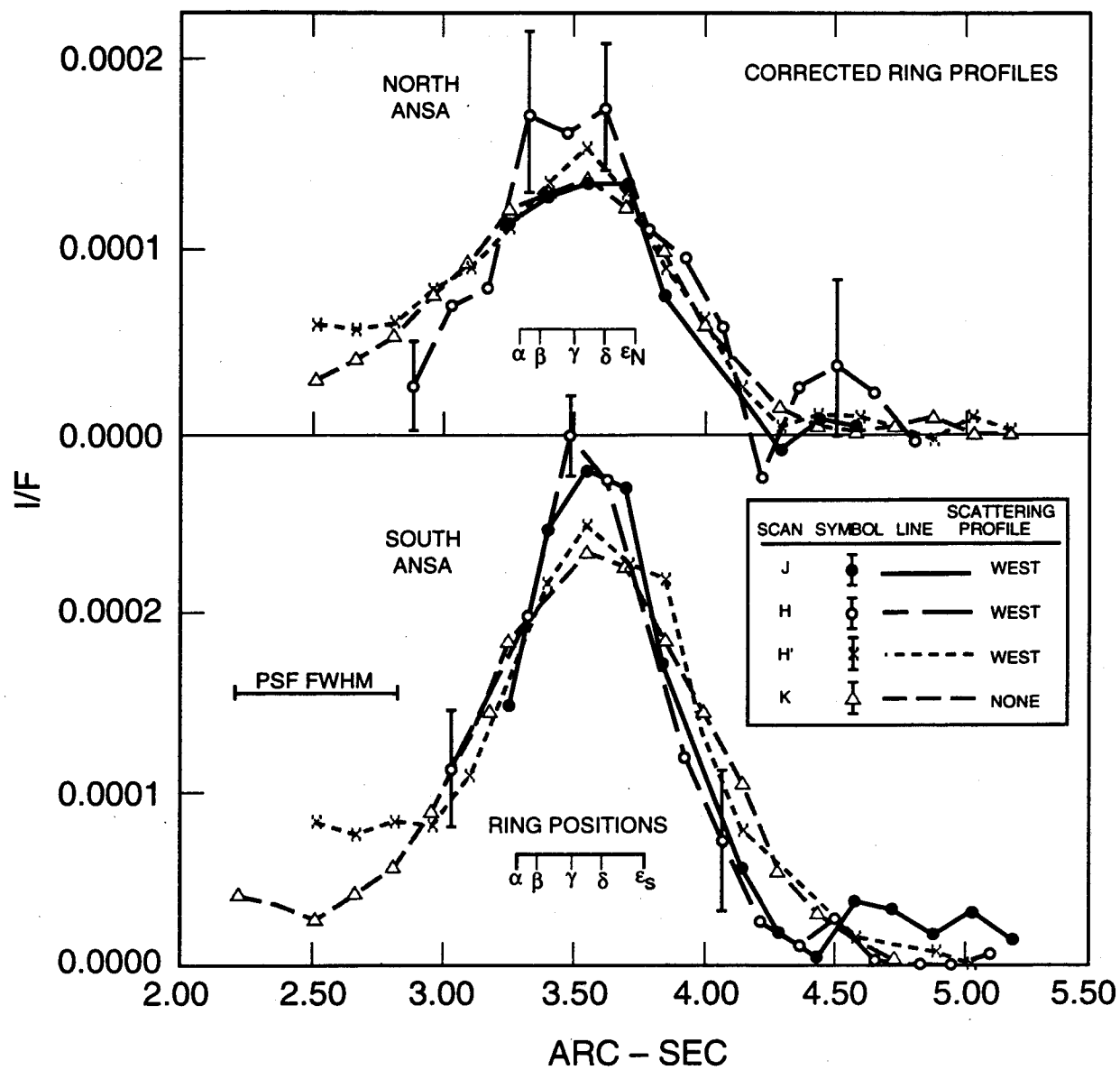


FIGURE 5

FIGURE 6



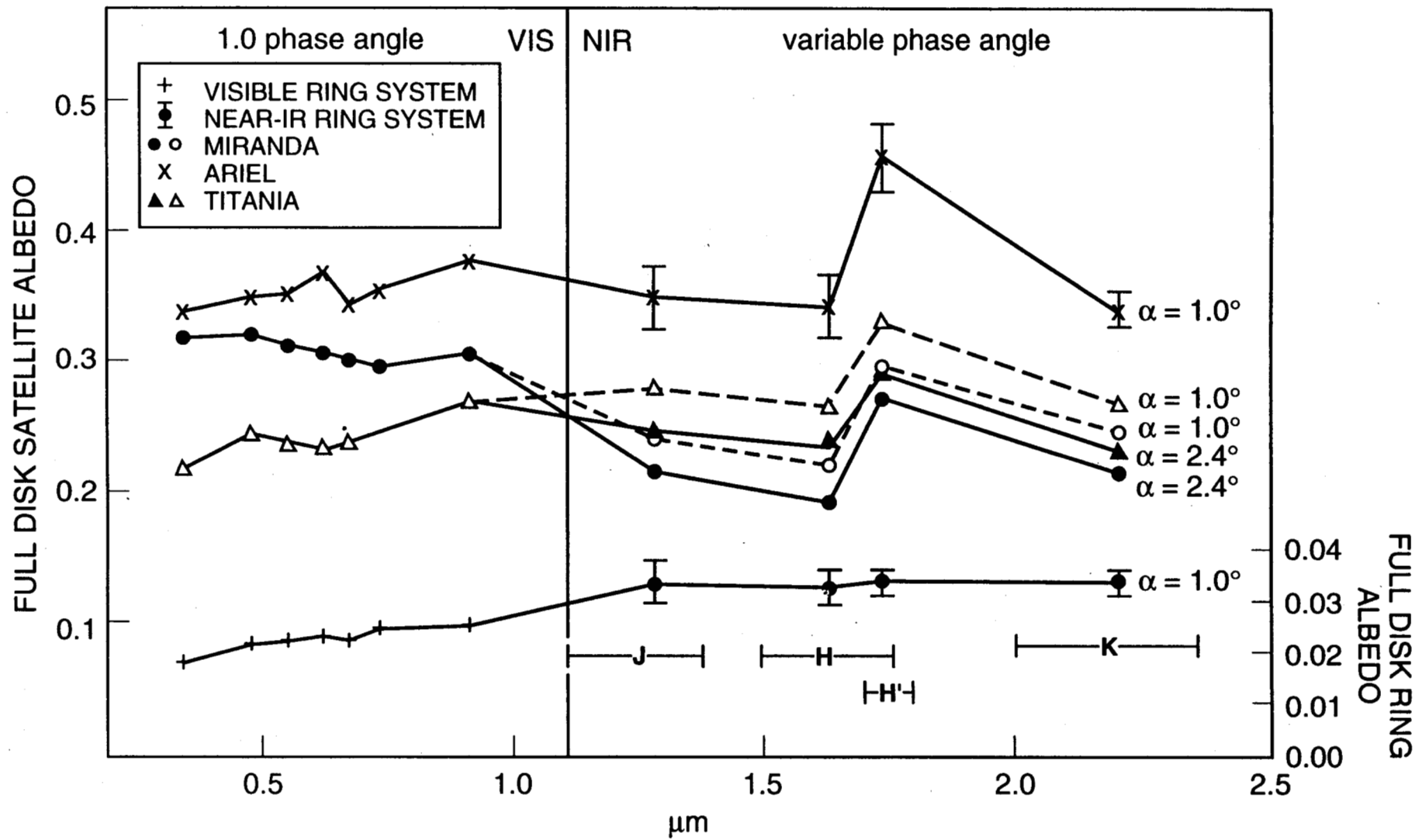


FIGURE 7

FIGURE 8

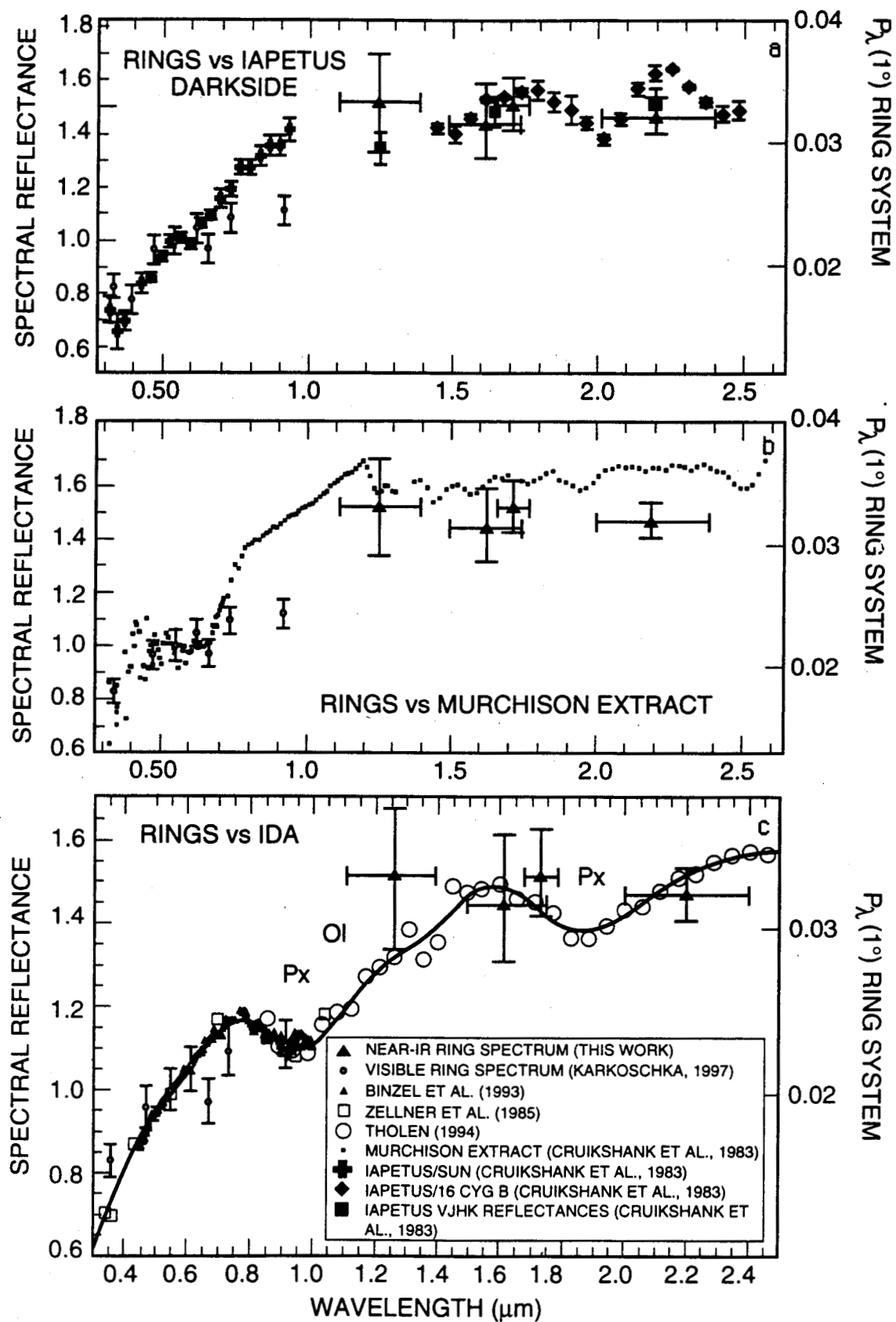


FIGURE 9

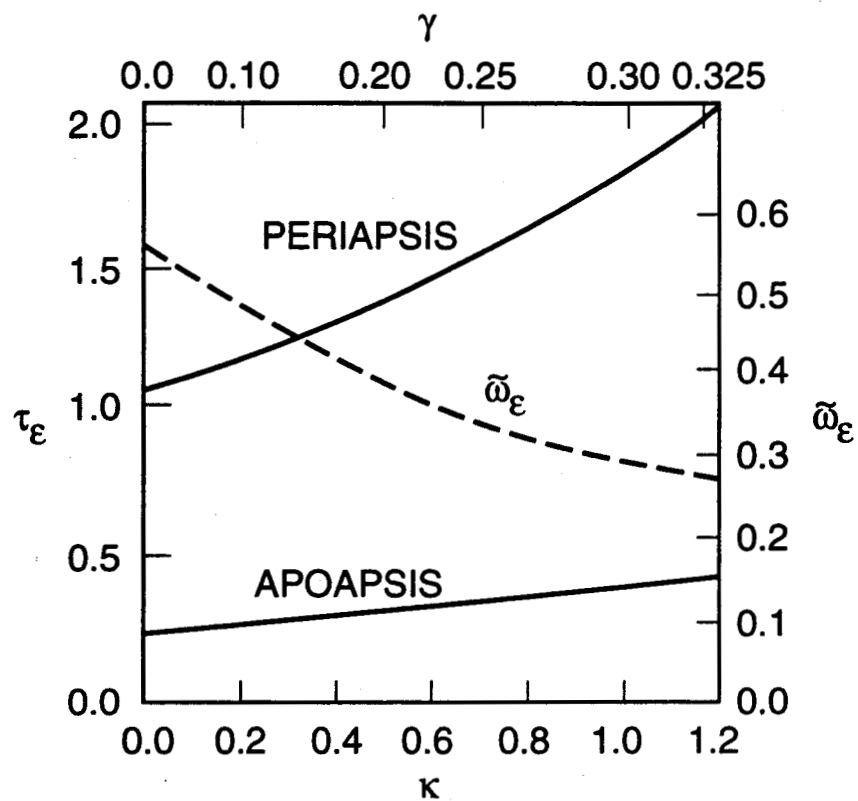


FIGURE 10

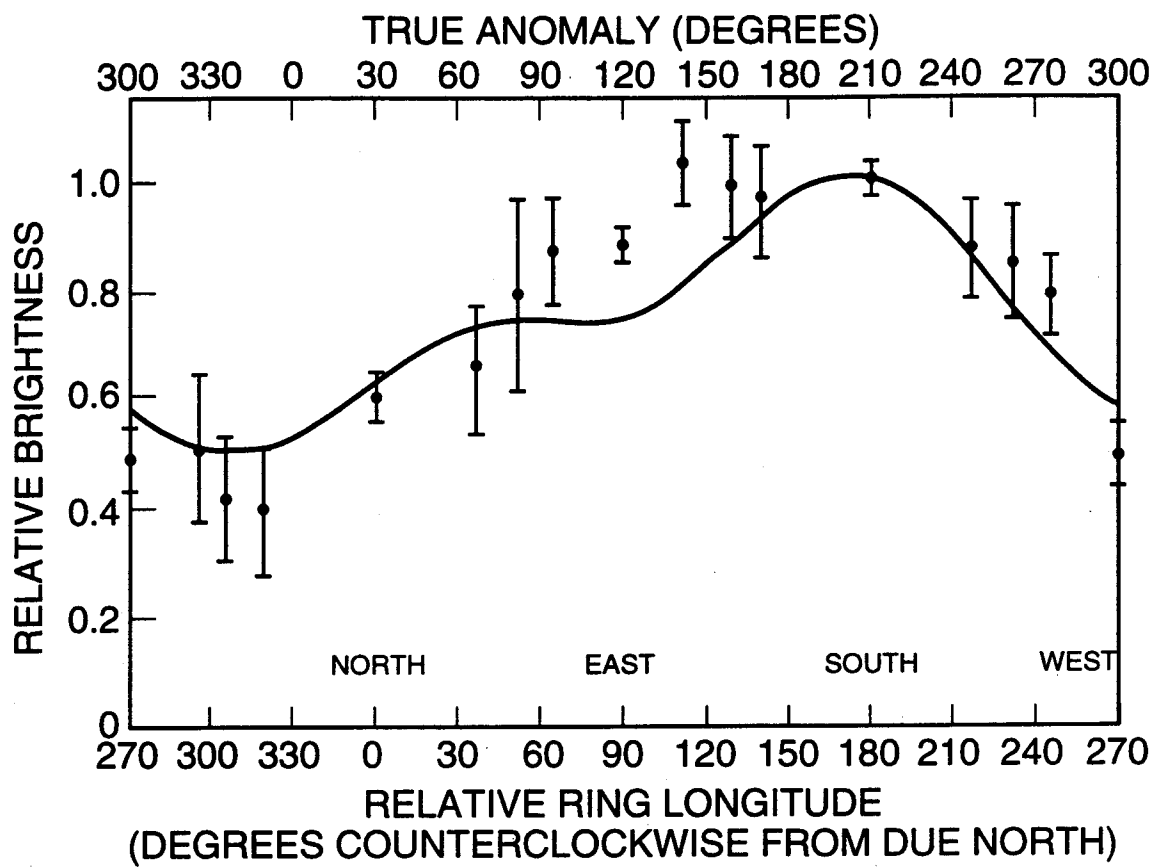


FIGURE 11

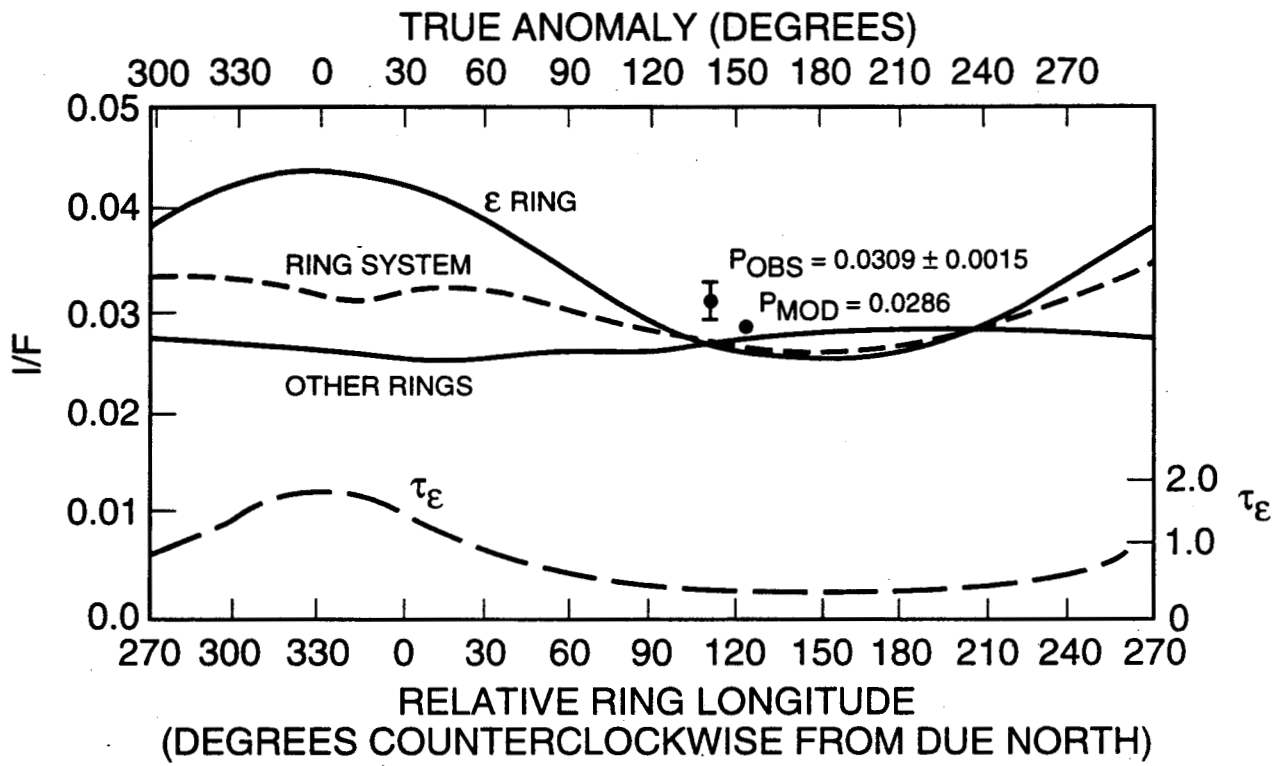


FIGURE 12

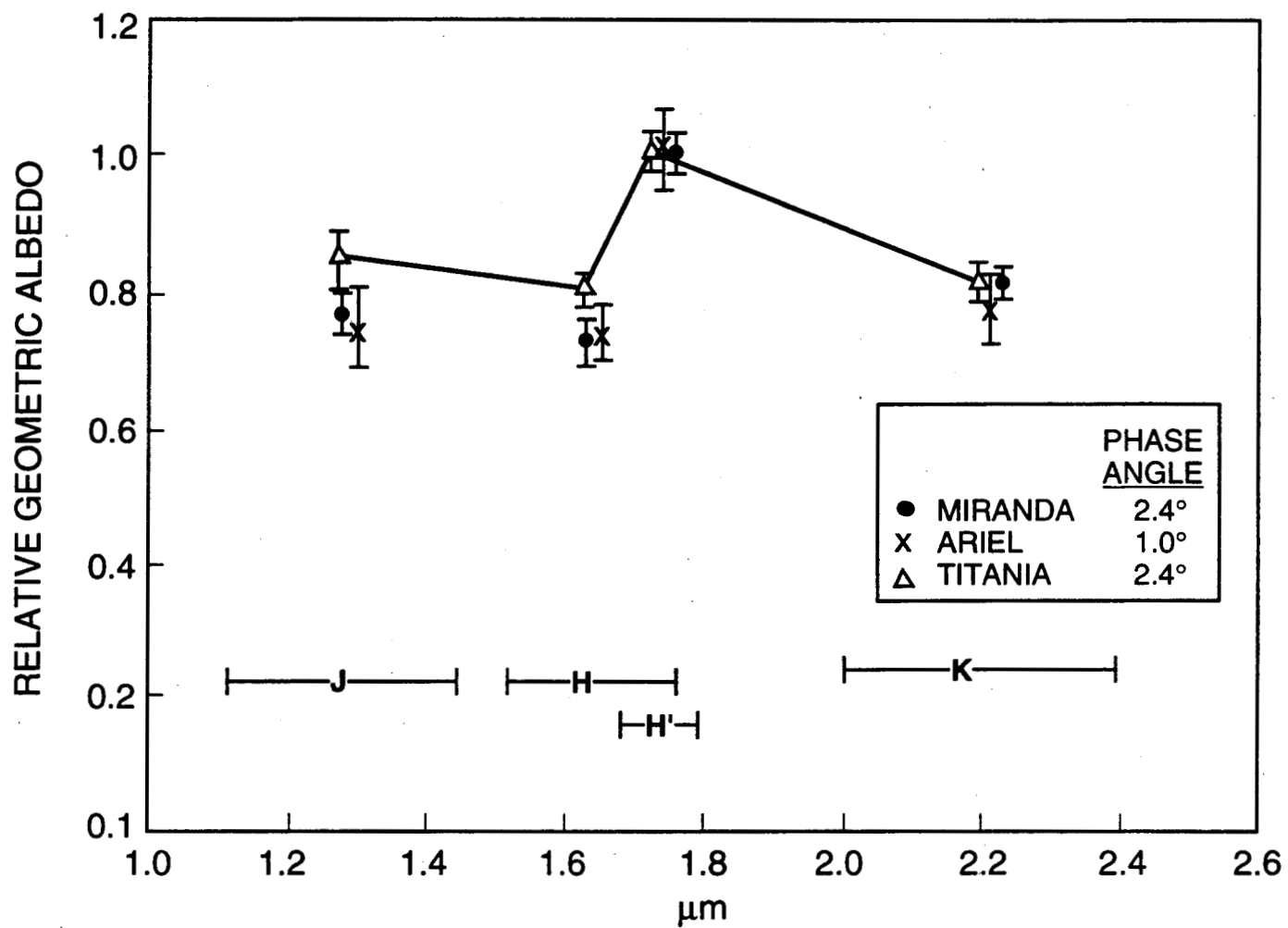


FIGURE 13

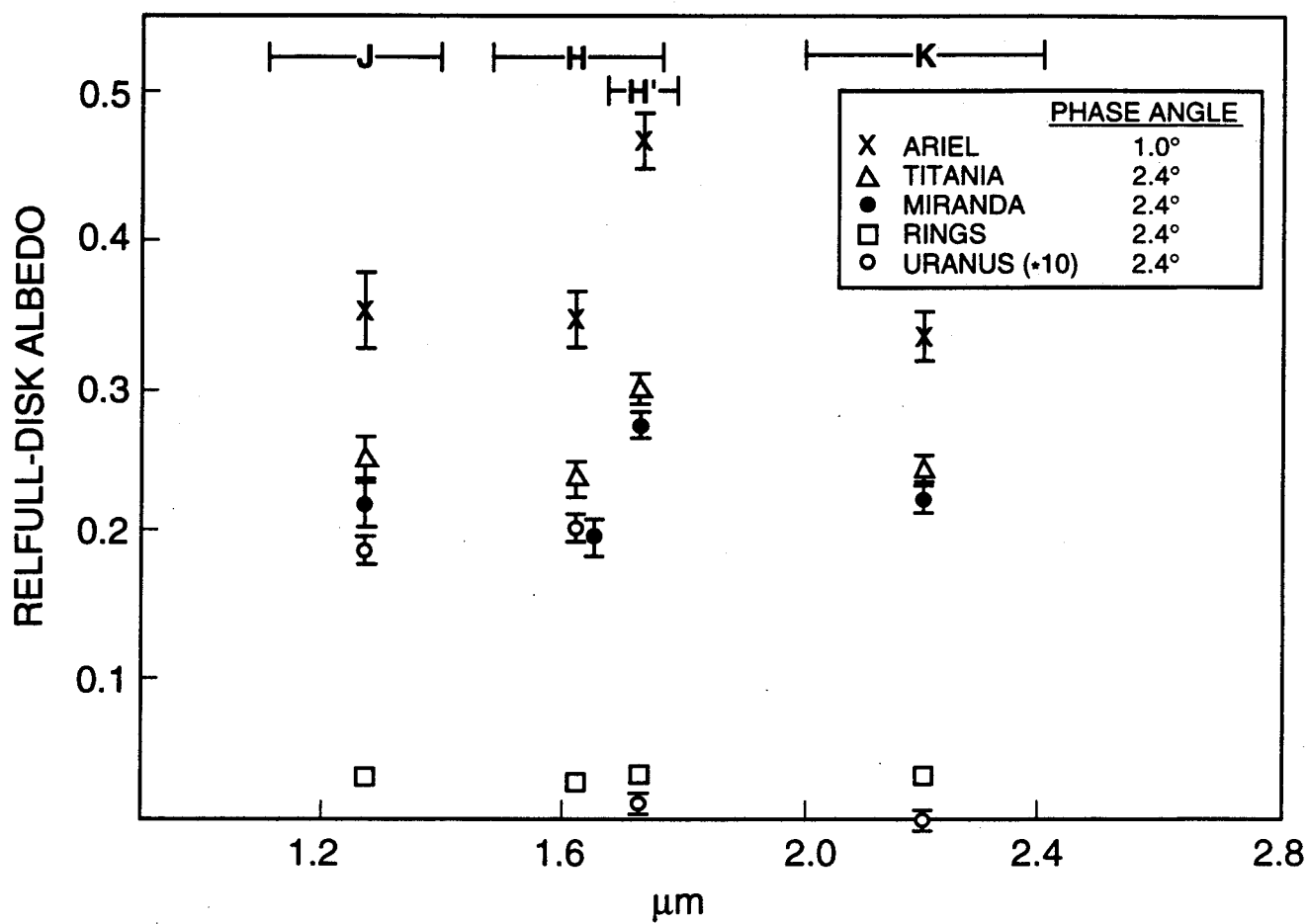
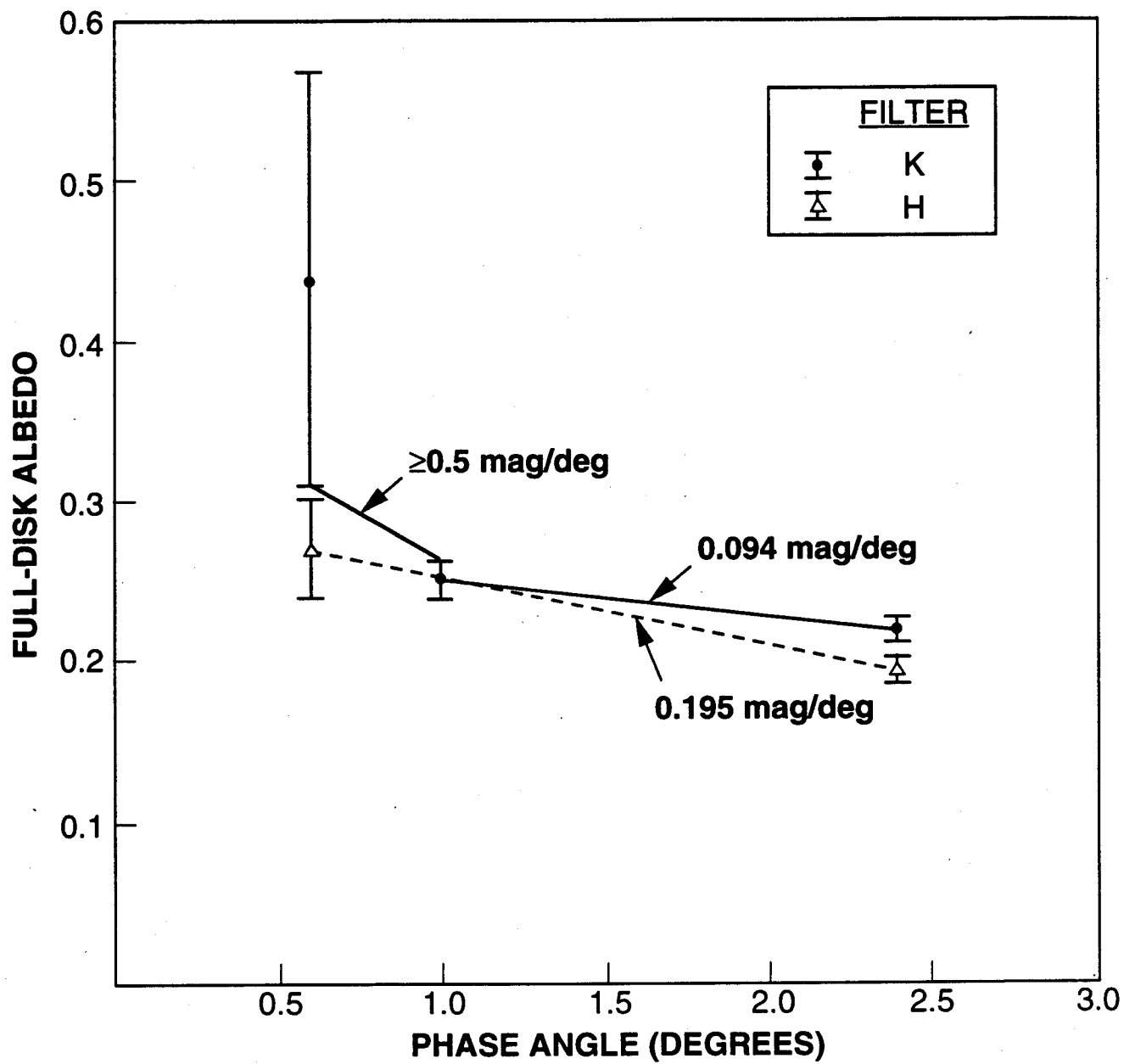


FIGURE 14



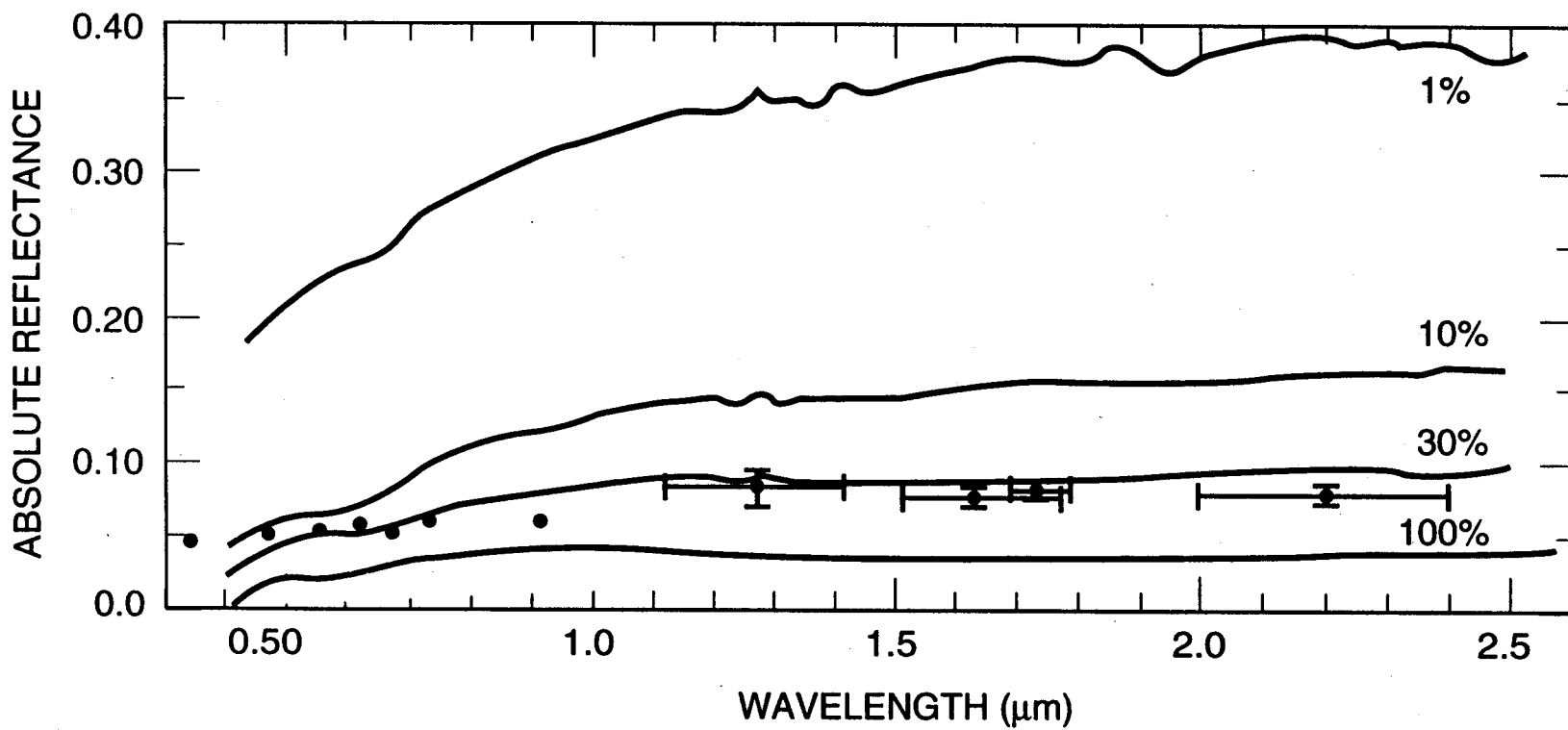


FIGURE 15